Spatial slip rate distribution along the SE Xianshuihe fault, eastern Tibet, and earthquake hazard assessment

Mingkun Bai[1,2], Marie-Luce Chevalier[1,3*], Philippe Hervé Leloup[4], Haibing Li[1,3], Jiawei Pan[1,3], Anne Replumaz[5], Shiguang Wang[6,1], Kaiyu Li[1], Qiong Wu[1], Fucai Liu[1], Jinjiang Zhang[2]

[1] Key Laboratory of Deep-Earth Dynamics of Ministry of Natural Resources, Institute of Geology, Chinese Academy of Geological Sciences, 26 Baiwanzhuang Rd, Beijing 100037, People's Republic of China

[2] Ministry of Education Key Laboratory of Orogenic Belts and Crustal Evolution, School of Earth and Space Sciences, Peking University, Beijing 100871, People's Republic of China

[3] Southern Marine Science and Engineering Guangdong Laboratory (Guangzhou), Guangzhou 511458, People's Republic of China

[4] Laboratoire de géologie de Lyon, CNRS UMR 5570, Université de Lyon, Villeurbanne, France

[5] ISTerre, Université Grenoble Alpes, CNRS, Grenoble, France

[6] National Institute of Natural Hazards, Ministry of Emergency Management of China, Beijing, China

Highlights

[*]Corresponding author : Marie-Luce Chevalier (mlchevalier@hotmail.com), Tel: +86 13466654223

-We determined late Quaternary slip rates of 3.7-5.4 and 10.4-14.8 mm/yr along the Zheduotang and Moxi segments, respectively

-We suggest a SE rate increase along the Xianshuihe fault system from Ganzi to Moxi

-We discovered a new active fault (Mugecuo South) between Selaha and Zheduotang segments, a large-scale pull-apart within an uplift zone

Abstract

The Xianshuihe (XSH) fault in eastern Tibet is one of the most active faults in China, with the next large earthquake most likely to occur along its SE part, where the fault splits into three parallel branches: Yalahe, Selaha and Zheduotang. Precisely quantifying their slip rates at various timescales is essential to evaluate regional earthquake hazard. Here, we expand our previous work on the Selaha fault, to the nearby Zheduotang and Moxi faults, and add observations on the Yalahe fault and on the newly discovered Mugecuo South fault zone. Using tectonic-geomorphology approaches with ^{10}Be dating, we had determined average late Quaternary slip rates of 9.75±0.15 and 4.4±0.5 mm/yr along the NW and SE Selaha fault, respectively. Using the same methods here, we determine a slip rate of 3.7-5.4 mm/yr on the Zheduotang fault and of 10.4-14.8 mm/yr on the Moxi fault. This is consistent with the southeastward slip rate increase we had proposed along the XSH fault system from 6-8 mm/yr (Ganzi fault) to ~10 mm/yr (Selaha fault), and >10.4 mm/yr (Moxi fault). We eventually propose a new model for the SE Xianshuihe fault, where the large-scale Mugecuo pull-apart basin lies within an even larger scale compressive uplift zone in the XSH fault's restraining bend, where the highest peak in eastern Tibet is located (Gongga Shan, 7556 m). Our slip rates determination allows to estimate a relatively high regional earthquake hazard of Mw~7 at present in the SE Xianshuihe fault.

Plain Language Summary

The Xianshuihe fault in eastern Tibet is one of the most active faults in China, with the next large earthquake most likely to occur along its southeastern part, where the fault zone consists of four parallel branches with complicated geometries. Studying the activity and slip rate of each branch is essential to evaluate regional earthquake hazard, especially because they cross a major city (Kangding), and because of the imminent construction of the Chengdu-Lhasa railroad. Here, we expand our previous slip rate study on one fault branch (Selaha) to two additional ones (Zheduotang and Moxi), together with key observations on the newly discovered 'Mugecuo South fault zone'. We find that the rate over the last ~100,000 years may increase southeastwards along the Xianshuihe fault system, as previously suggested. The fast slip rates and their complex spatial distribution in the Kangding region reveal a high earthquake hazard (Mw~7) at present.

1. Introduction

The eastern margin of the Tibetan Plateau is an important, active tectonic boundary with numerous active faults which accommodate slip due to the eastward motion of the plateau (e.g., Tapponnier and Molnar, 1977; Wang et al., 1998; Wang and Burchfiel, 2000; Han et al., 2019) (Fig. 1). This region belongs to the "eastern Tibet seismic belt" or "N-S tectonic zone" (Deng et al., 2003; Zhang, 2013) along which an extremely large number of M>7 earthquakes occurred. In particular, along the NW-striking, ~1400 km-long, left-lateral Xianshuihe (hereafter XSH) fault system, as many as 17 M>7 and 29 M>6.5 earthquakes have ruptured almost its entire length since 1700, with three M>7.3 earthquakes along just the XSH segment since 1923 (Allen et al., 1991; Wen, 2000) (Fig. 2A). Following two large earthquakes nearby (2008 Mw7.9 Wenchuan and 2013 Ms7 Lushan, Fig. 1), the seismic risk near Kangding city is believed to have increased by a factor of two, attested by Coulomb stress increase (e.g., Parsons et al., 2008; Toda et al., 2008; Shan et al., 2009, 2013; Nalbant and McCloskey, 2011; Yang et al., 2015; Guo et al., 2018; Xu et al., 2019), which was only

69 partly reduced after the 2014 Kangding earthquake sequence (Mw5.9 and 5.6) (Jiang et al 2015a;
70 Bai et al., 2018) (Fig. 2A). This region is now widely accepted as a seismic gap (e.g., Allen et al.,
71 1991; Wen, 2000; Wen et al., 2008; Jiang et al., 2015a; Shao et al., 2016; Wang and Shen, 2020; Li
72 and Bürgmann, 2021), where a large earthquake would be tragic because of casualties (Kangding
73 city has a population of ~150,000) and infrastructure damages not only due to ground shaking but
74 also because of landslides and mud flows on the very steep surrounding slopes.

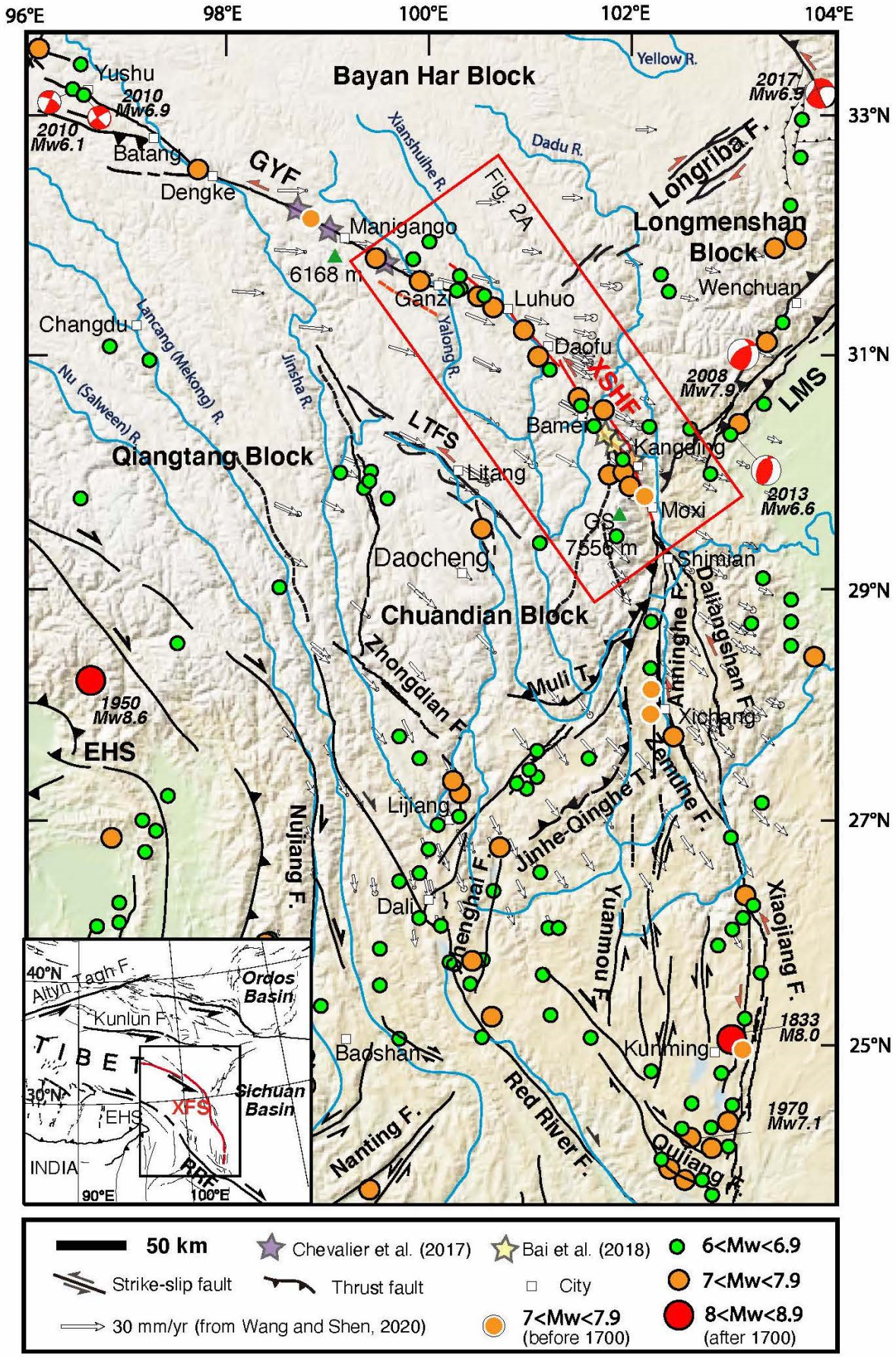
96°E
98°E
100°E
102°E
104°E
33°N
31°N
29°N
27°N
25°N
Bayan Har Block
Yellow R.
Yushu
2010 Mw6.9
2010 Mw6.1
Batang
Dengke
GYF
Manigango
6168 m
Ganzi
Luhuo
Yalong R.
Xianshuihe R.
Dadu R.
Fig. 2A
Longriba F.
Longmenshan Block
Wenchuan
2017 Mw6.5
Changdu
Lancang (Mekong) R.
Nu (Salween) R.
Jinsha R.
Daofu
XSHF
2008 Mw7.9
LMS
Bame
Kangding
LTFS
Litang
Qiangtang Block
2013 Mw6.6
Moxi
GS
7556 m
Shimian
Daocheng
Chuandian Block
Dalianghe F.
Dalangshan F.
Zhongdian F.
Muli T.
Anninghe F.
1950 Mw8.6
EHS
Xichang
Lijiang
Jinhe-Qinghe T.
Zemuhe F.
Nujiang F.
Dali
Chenghai F.
Yuanmou F.
Xiaojiang F.
1833 M8.0
Kunming
Baoshan
Red River F.
Nanting F.
1970 Mw7.1
Qujiang F.
40°N
Altyn Tagh F.
Ordos Basin
Kunlun F.
TIBET
30°N
EHS
XFS
Sichuan Basin
INDIA
RRF
90°E
100°E
50 km
Chevalier et al. (2017)
Bai et al. (2018)
6<Mw<6.9
Strike-slip fault
Thrust fault
City
7<Mw<7.9
30 mm/yr (from Wang and Shen, 2020)
7<Mw<7.9 (before 1700)
8<Mw<8.9 (after 1700)

Figure 1: *Xianshuihe fault system (XFS) within India–Asia collision zone. Tectonic map of SE Tibet with digital elevation model (DEM) in background. Horizontal GPS velocity field with respect to stable Eurasian plate (Wang and Shen, 2020), focal mechanisms of instrumental, Mw>6 earthquakes (Global Harvard CMT catalog 1976–2020) (2008 Wenchuan, 2010 Yushu, 2013 Lushan and 2017 Jiuzhaigou), as well as earthquakes from USGS and CEA (1995), main peaks, cities, active faults (those of Xianshuihe fault in red), tectonic blocks and rivers. LMS=Longmenshan, GYF=Ganzi-Yushu fault, XSHF=Xianshuihe fault, LTFS=Litang fault system, GS=Gongga Shan. Inset shows the XFS within Asia, EHS=Eastern Himalayan Syntaxis, RRF=Red River fault.*

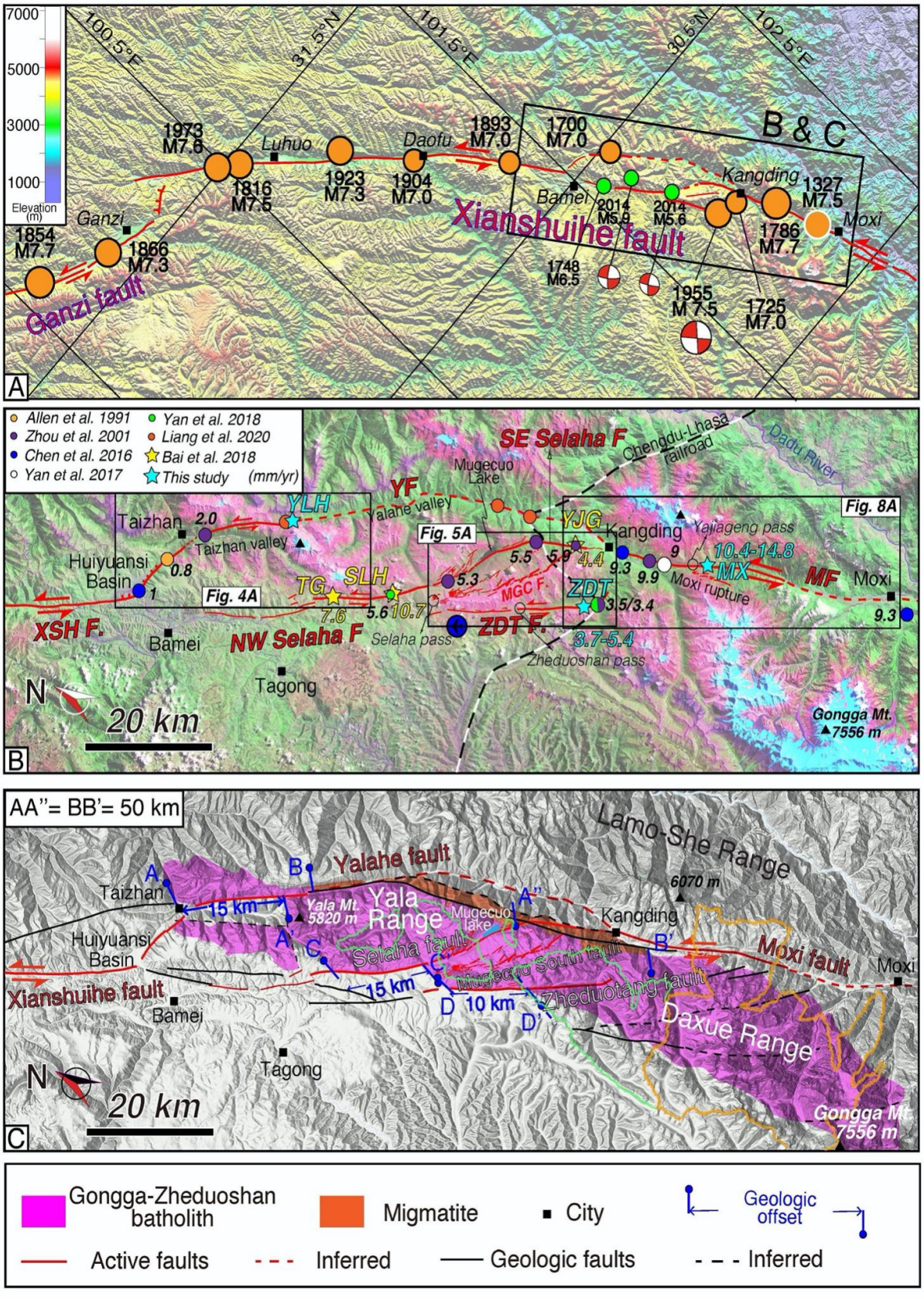

Figure 2: *Xianshuihe (XSH) fault. (A) Post 1700 A.D. M>7 earthquakes distribution (+ that of 1327 near Moxi) (e.g., USGS, Wen et al., 2008; Cheng et al., 2011) along XSH and SE Ganzi faults.*

Focal mechanisms from Jiang et al. (2015a) and Lin et al. (1986). (B) Landsat satellite image of SE XSH fault (box in A), where main trace splays into Yalahe (YF), Selaha (NW and SE) and Zheduotang (ZDTF) segments before reconnecting as Moxi fault (MF) farther to SE. MGCF=Mugecuo South fault. Location of main geographic and topographic features indicated, in addition to approximate location of study sites and late Quaternary (average) slip rates from others. (C) Simplified geologic map of SE segment of XSH fault, with Gongga-Zheduoshan batholith and its geologic offsets (following Liu et al., 1977; Chen et al., 1985). Green and orange contours represent moderate (<0.9 mm/yr) and high (0.9 - 7.6 mm/yr) ^{10}Be basin-wide erosion rates, respectively (Ouimet et al., 2009; Cook et al., 2018).

Near Kangding city, the linear XSH fault splits into three right-stepping, en-echelon segments: Yalahe, Selaha and Zheduotang, before reconnecting as the Moxi segment (Fig. 2B). In order to better understand the complicated tectonics of this particularly active region of eastern Tibet, and assess its seismic hazard, precisely constraining the slip-rates of the several regional active fault branches is essential. While Bai et al. (2018) determined the Selaha fault's late Quaternary horizontal slip-rate at three locations, in this paper, we constrain that of two other regional fault segments (Zheduotang and Moxi) using similar approaches (see method section). We also present preliminary observations on the activity of the central Yalahe segment, as well as of that of the newly discovered 'Mugecuo South' fault zone located between the Selaha and Zheduotang segments, which documents significant extension. Finally, we discuss the rates distribution in the Kangding region of the SE XSH fault in the framework of eastern Tibet and compare them with those from other regional studies at all timescales. We eventually propose a model for the SE XSH fault where a large-scale pull-apart basin (Mugecuo) lies within an even larger scale restraining bend where the highest peak in eastern Tibet is located (Gongga Shan, 7556 m), and assess regional seismic hazard using the slip rates we determined. Our work also provides valuable data to the highly challenging Chengdu-Lhasa railroad construction, which will cross all fault segments discussed here (Fig. 2B).

2. Geological setting

The XSH fault system consists of four main left-lateral strike-slip fault segments which separate the Bayan Har and Qiangtang/Chuandian blocks to the NE and SW, respectively: Yushu/Batang at the NW end (where the 2010 Mw6.9 Yushu earthquake occurred), Ganzi in the NW, XSH and Moxi in the center, and Anninghe-Zemuhe-Xiaojiang in the SE (Fig. 1). In the Kangding region, the Yalahe, Selaha and Zheduotang segments follow geological faults that left-laterally offset the Gongga-Zheduoshan granite batholith (Chen et al., 1985) (Fig. 2C) and may be connected at depth (e.g., Allen et al., 1991; Jiang et al., 2015a; Li et al., 2020). While the Selaha and Zheduotang faults show evidence of recent activity along most of their traces, with numerous scarps, sag ponds, and left-lateral (with minor vertical) offsets of mostly moraines and gullies, such clear evidence seemed to be lacking along the Yalahe fault where it is parallel to the Selaha fault (Allen et al., 1991; Bai et al., 2018).

2.1. Slip rates review

As slip-rates may vary temporally and/or spatially along a particular fault (e.g., Friedrich et al., 2003; Chevalier et al., 2005), it is important to estimate them at various timescales as summarized below as well as in Figure 3 and Table 1, from a few tens of years (using geodetic techniques such as GPS/GNSS [Global Satellite Navigation System] or InSAR [Interferometric Synthetic Aperture Radar]), to a few tens of ka (using tectonic-geomorphology approaches), to a few Ma (using geologic tools).

2.1.1. Geologic timescale

Geologic rate estimates along the XSH fault vary between ~3.5 and 30 mm/yr, depending on whether the ~60 km geologic offset of several markers (Jinsha and Xianshui Rivers, Proterozoic and Permo-Triassic basement rocks, main Cenozoic thrusts) (e.g., Wang et al., 1998; Wang and Burchfiel, 2000; Yan and Lin, 2015) is matched with initiation ages that vary from 2 to 19 Ma (e.g.,

142 Roger et al., 1995; Wang et al., 1998; Wang et al., 2012; Zhang, 2013; Yan and Lin, 2015; Zhang et
143 al., 2017).

144

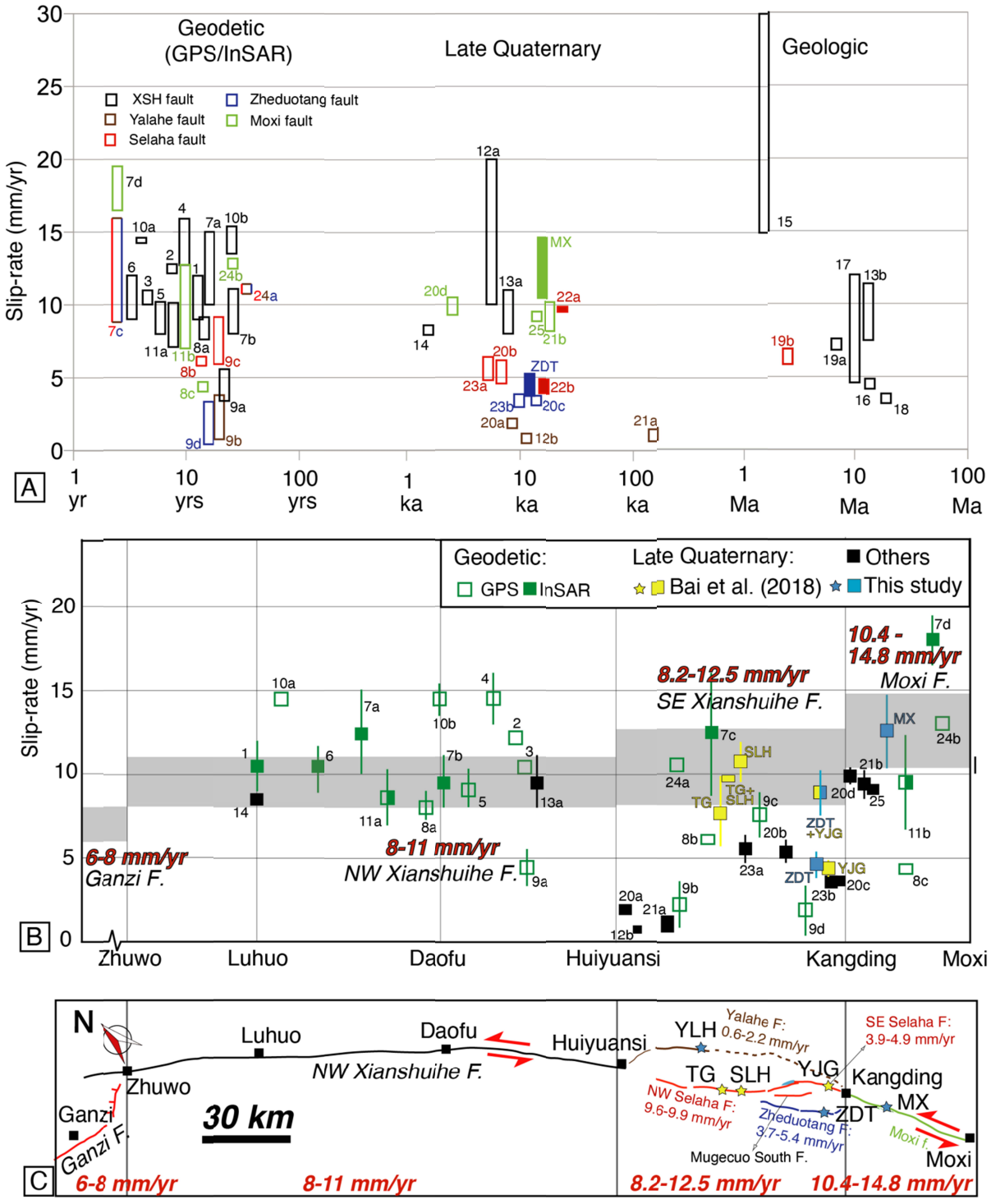

145

146 ***Figure 3:*** *Summary of left-lateral slip rates along Xianshuihe and Moxi faults versus time (A) and*

location along strike (B). See Table 1 for references to numbers. Colors represent rates along different segments. Plain symbols represent our rates (this study as well as that of Bai et al., 2018). (B) Grey shaded areas represent the best constrained late Quaternary rates for each main section of the XSH fault: Ganzi, NW XSH, SE XSH, and Moxi faults (see discussion section). (C) Fault trace, main cities and location of our study sites (blue stars: this study; yellow stars: Bai et al., 2018), with best constrained late Quaternary slip rates in red (that of Ganzi from Chevalier et al., 2017).

Table 1: *Slip rate summary along Xianshuihe fault*

Segment	Slip-rate (mm/yr)	Reference	Method	Ref. in Fig. 3
XSH fault	*9 - 12*	Wang et al. (2009)	InSAR near Luhuo	1
	12.2 - 13	W. Wang et al. (2017)	GPS - block model	2
	10 - 11	Shen et al. (2005)	GPS - rigid blocks	3
	12.7 - 15.9	Y. Wang et al. (2017)	GPS - block model	4
	8 - 10.2	Zheng et al. (2017)	GPS - profiles	5
	9 - 12	Ji et al. (2020)	InSAR - interseismic deformation	6
	10 - 15	Zhang et al. (2019)	InSAR - dislocation model	7a
	8.1-11.1	Qiao and Zhou (2021)	InSAR	7b
	7.67 - 9.13	Li et al. (2019)	Gravity + GPS (Luohuo-Qianning)	8a
	3.4 - 5.6	Li et al. (2020)	GPS + earthquake relocation (Daofu-Qianning)	9a
	14.4	Gan et al. (2007)	GPS - dislocation	10a
	13.6-15.4	Wang et al. (2020)	GPS - elastic block model	10b
	7 - 10.3	Jiang et al. (2015b)	3D visco-elastic model with InSAR and GPS data	11a
	10 - 20	Allen et al. (1991)	inferred ages	12a
	8 - 11	Zhang (2013)	reinterpretation of Chen et al. (2008), using upper terrace age	13a
	8.4	Liang et al. (2020)	14C - Paleoearthquake 3 ka (Luhuo)	14
	7.5 - 11.1	Zhang (2013)	90 - 100 km in 10 Ma	13b
	15 - 30	Wang et al. (1998)	60 km in 2-4 Ma	15
	~4.5	Roger et al. (1995)	62 km in 13 Ma (Bai et al., 2018)	16
	4.6 - 12	Yan and Lin (2015)	62 km in 5-13 Ma	17
	~3.5	Wang et al. (2012)	62 km in 17±2 Ma (Bai et al., 2018)	18
	6.8 - 7.6	Zhang et al. (2017)	62 km since 8.6±0.5 Ma	19a
Yalahe fault	*0.8 - 3.8*	Li et al. (2020)	GPS + earthquake relocation	9b

	0.8	Allen et al. (1991)	inferred ages	12b
	1.8 - 2.2	Zhou et al. (2001)	one TL age - paleoseimology	20a
	0.6 - 1.5	Chen et al. (2016)	TL ages - tectonic geomorphology	21a
Selaha fault	*6.14*	Li et al. (2019)	Gravity + GPS data	8b
	5.9 - 9.1	Li et al. (2020)	GPS + earthquake relocation	9c
	4.9 - 6.1	Zhou et al. (2001)	TL and 14C ages - paleoseimology	20b
	9.6 - 9.9	**Bai et al. (2018)**	**10Be (TG and SLH sites, NW Selaha fault)**	**22a**
	3.9 - 4.9	**Bai et al. (2018)**	**10Be (YJG site, SE Selaha fault)**	**22b**
	4.8 - 6.4	Yan et al. (2018)	14C - tectonic geomorphology	23a
	5.7 - 6.9	Zhang et al. (2017)	25 km since 4±0.4 Ma (Bai et al., 2018)	19b
Zheduotang fault	*0.4 - 3.4*	Li et al. (2020)	GPS + earthquake relocation	9d
	3.2 - 3.8	Zhou et al. (2001)	14C - paleoseimology	20c
	3 - 3.8	Yan et al. (2018)	14C - tectonic geomorphology	23b
	3.7 - 5.4	**This study**	**10Be (ZDT site)**	**ZDT**
Yalahe/Selaha/Zheduotang	*~11*	Wang and Shen (2020)	GPS - profiles	24a
	8.8-16	Qiao and Zhou (2021)	InSAR	7c
Moxi fault	*7 - 12.7*	Jiang et al. (2015b)	3D visco-elastic model with InSAR and GPS data	11b
	4.41	Li et al. (2019)	Gravity and GPS data	8c
	~13	Wang and Shen (2020)	GPS - profiles	24b
	16.5-19.3	Qiao and Zhou (2021)	InSAR	7d
	9.3 - 10.5	Zhou et al. (2001)	14C - paleoseimology	20d
	8.3 - 10.3	Chen et al. (2016)	14C - tectonic geomorphology	21b
	~9	Yan et al. (2017)	14C - paleoseimology	25
	10.4 - 14.8	**This study**	**10Be (MX site)**	**MX**

2.1.2. Late Quaternary timescale

A growing body of evidence now suggests a slip rate of ~10 mm/yr for the XSH fault (e.g., Zhang, 2013; Bai et al., 2018). Bai et al. (2018) suggested that the southeastward rate increase between the Ganzi fault (~6-8 mm/yr, Chevalier et al., 2017) and the XSH fault may be linked to the interaction with the nearby NE-striking, reverse/dextral Longriba fault system to the north, as recently endorsed by a recent GPS study (Wang et al., 2020). This fault indeed marks the limit between the fast-moving Bayan Har block to the NW and the slow-moving Longmenshan block to

163 the SE, as observed in GPS data when considered relative to stable Eurasia (e.g., W. Wang et al.
164 2017, 2020; Y. Wang et al., 2017; Wang and Shen, 2020) (Fig. 1).

165 What occurs in the Kangding region however, where the fault splits into three segments, is
166 more complex. While the NW Yalahe fault, with a normal/left-lateral sense consistent with its
167 oblique direction compared to the general trend of the geologic fault, may slip at ~0.6 to 2.2 mm/yr
168 (Allen et al., 1991; Zhou et al., 2001; Chen et al., 2016, Figs. 2B, 3, and Table 1), no rates have yet
169 been determined farther to the SE. Along the NW Selaha fault (west of the Selaha pass, Fig. 2B),
170 slip rates had been inferred to range between 3.7 and 9.7 mm/yr (Allen et al., 1991; Chen et al.,
171 2016) and were estimated (using ^{14}C dating) as ranging from 4.8 to 6. 4 mm/yr (Zhou et al., 2001;
172 Yan et al., 2018). More recently, Bai et al. (2018) studied two sites along the NW Selaha fault (TG
173 and SLH) and one site along its SE part (YJG) (yellow stars in Fig. 2B). Using ^{10}Be dating and
174 offset-age reconstructions, they determined slip-rates of 7.6(+2.3/−1.9) mm/yr at TG and
175 10.7(+1.3/−1.1) mm/yr at SLH, hence 9.6 - 9.9 mm/yr assuming that the rate should be similar at
176 these two sites located only 9 km apart. At YJG, located along the SE Selaha fault, Bai et al. (2018)
177 determined a much lower rate of 3.9 - 4.9 mm/yr. This led them to infer a rate of ~5 mm/yr on the
178 parallel Zheduotang fault, corresponding to the difference between rates along the NW and SE
179 Selaha fault. Other studies on the Zheduotang fault suggested slip-rates of 3 to 3.8 mm/yr (Zhou et
180 al., 2001; Yan et al., 2018) (Figs. 2B, 3, and Table 1).

181 The linear and continuous, ~50 km-long, Moxi fault located SE of Kangding, merges with the
182 Selaha fault (Allen et al., 1991; Jiang et al., 2015a; Bai et al., 2018). Most studies used ^{14}C dating
183 from trenches located <9 km from Kangding, NW of the Yajiageng (or Xuemenkan) pass (Fig. 2B),
184 to determine late Quaternary slip-rates along the Moxi fault of ~8.3-10.5 mm/yr (e.g., Zhou et al.,
185 2001; Chen et al., 2016; Yan et al., 2017).

186 **2.1.3. Geodetic timescale**

187 At the geodetic timescale, InSAR (7-15 mm/yr, e.g., Wang et al., 2009; Jiang et al., 2015b;
188 Zhang et al., 2019; Ji et al., 2020; Qiao and Zhou, 2021) and GPS (8-15.9 mm/yr, e.g., Shen et al.
189 2005; Gan et al., 2007; W. Wang et al., 2017, 2020; Y. Wang et al., 2017; Zheng et al., 2017; Li et
190 al., 2019) rates along the XSH fault (Fig. 3 and Table 1) are widespread but encompass the late
191 Quaternary rates. Note however that estimates based on the longest GPS record (Zheng et al., 2017)
192 suggest a rate of ~8 to 10.2 mm/yr. At a more detailed level, GPS rates vary between 0.8 and 3.8
193 mm/yr along the Yalahe fault (Li et al., 2020), 5.9-9.1 mm/yr along the Selaha fault (Li et al., 2019;
194 Li et al., 2020), 0.4-3.4 mm/yr along the Zheduotang fault (Li et al., 2020) and 4.41-19.3 mm/yr
195 along the Moxi fault (Jiang et al., 2015b; Li et al., 2019; Wang and Shen, 2020; Qiao and Zhou,
196 2021). Two recent studies recently suggested rates of ~11 mm/yr (Wang and Shen, 2020) and 8.8-16
197 mm/yr (Qiao and Zhou, 2021) across the three branches (Yalahe/Selaha/Zheduotang) of the SE
198 XSH fault (Fig. 3 and Table 1).
199

200 **2.2. Past earthquakes in the Kangding region**

201 One M7.0 earthquake in 1700 has been reported along the Yalahe fault with ~41 km of surface
202 ruptures (Wen, 2000; Wen et al., 2008) (Fig. 2A). Two historical earthquakes, M7.0 in 1725 and
203 M6.5 in 1748, have both been inferred to have ~40 km of surface ruptures along the SE and NW
204 Selaha fault, respectively, the former being however poorly constrained (Wen, 2000; Wen et al.,
205 2008; Papadimitriou et al., 2004). The recent 2014 Mw5.9 and 5.6 Kangding earthquake sequence
206 also mostly shook the NW part of that fault (e.g., Jiang et al., 2015a). Along the Zheduotang fault,
207 the 1955 Mw7.5 Kangding earthquake produced 35 km of surface ruptures (Wen, 2000; Wen et al.,
208 2008; Zhou et al., 2001; Papadimitriou et al., 2004), although it has recently been re-evaluated by
209 Yan et al. (2019) as only Mw7.0 with 43 km of surface ruptures that extend farther SE towards
210 Moxi ('Moxi rupture' in Fig. 2B). Along the Moxi fault, two large M7.5 and M7.7 earthquakes
211 occurred in 1327 and 1786, respectively, the latter having produced 70-90 km of surface ruptures

and 2-5 m of co-seismic offsets (Zhou et al., 2001; Wen et al., 2008; Cheng et al., 2011). It also yielded a landslide dam across the nearby Dadu River, whose rupture ten days later following a strong aftershock, caused one of the most disastrous landslide dam failure in the world with ~100,000 casualties (e.g., Dai et al., 2005).

3. Methods

We used field investigation, as well as Google Earth and Bing high-resolution satellite imagery to map active fault strands and offset geomorphic features along the Zheduotang and Moxi fault segments of the SE XSH fault near Kangding. We could then select the best sites with limited signs of erosion and clear piercing points across the fault in order to precisely measure the cumulative offsets. In this high elevation and high-relief region (with slopes up to 35° along the Zheduotang fault and 15° along the Moxi fault at our study sites), moraines and gullies are the most commonly observed offset markers, in addition to related sag ponds and fault scarps. Good sites are scarce. We selected the best two sites along the fault segments to conduct our study: the Zheduotang (ZDT) and Moxi (MX) moraines. That their crests are sub-rounded and oblique to the fault results in larger offset uncertainties, that we precisely measure on high-resolution Digital Elevation Models (DEM) obtained from Unmanned Aerial Vehicle (UAV aka drone, DJI Phantom 4 Pro) surveys at both sites, and from additional surveys using a Riegel VZ1000 terrestrial LiDAR (Light Detection and Ranging) (angular resolution of 0.02° for raw data, set to 0.5 m between two data points after process) at the MX site. Offset values and their uncertainties were obtained by repeatedly realigning the offset moraine crests to their best original fit on the DEM. Note that along a left-lateral fault, offsets on the left bank best represent the total offset, as that on the right bank may suffer continuous lateral erosion thus only yielding a minimum offset.

We therefore collected a total of 25 samples along the crests on the left bank: nine samples from the lateral moraine crest at the ZDT site and 11 from that at the MX site. These samples were

collected from the top few centimeters of large, stable, well-embedded granite boulders (1-4 m in diameter, Figs. S1-S2) using chisel and hammer. Collecting numerous (>6) samples on individual moraine crests has long been our team's moto, which greatly increases the likelihood to date the actual abandonment age of the moraine (Chevalier et al., 2011; Chevalier and Replumaz, 2019). Because moraines can only become stable after the ice retreats, their ages represent abandonment ages thus onset age of deglaciation.

We use cosmogenic ^{10}Be surface-exposure dating (e.g., Lal, 1991; Gosse and Phillips, 2001) to constrain the moraine abandonment ages following mineral separation and quartz cleaning procedure modified from Kohl and Nishiizumi (1992). ^{10}Be concentrations mostly come from nuclide accumulation from exposure to cosmic rays at the site. Model ages were calculated using CRONUS v3 (Balco et al., 2008) with the Lm (Lal [1991]/Stone [2000], time-dependent) and LSDn (Lifton et al., 2014, time-dependent) production rate models (Table 2) and we refer to the Lm ages in the text. We then combine the moraines abandonment age with their offsets to reconstruct the space-time evolution of the Zheduotang and Moxi faults and determine their late Quaternary average slip-rates. We report the latter as median rates (with uncertainties at the 68.27% confidence interval about the median) obtained using the Gaussian uncertainty model of Zechar and Frankel (2009).

Ideally, one wants to sample boulders that have been exposed on moraine crests since deglaciation, with no rolling, shielding or surface erosion since deposition (which would tend to skew the ages toward values younger than the actual age), and no exposure prior to deposition (which would tend to skew ages toward older values). These old ages however, are thought to be occasional (e.g., Hallet and Pukonen, 1994; Putkonen and Swanson, 2003; Heyman et al., 2011), especially since rocks have been pulled off from the glacial valley by the glacier, crushed, and eroded before resting on a moraine's crest. Such outliers may be singled out and discarded using statistical tests such as Chauvenet (Bevington and Robinson, 2002) or Peirce criteria. Four (three

young and one old) outliers were found on MX main crest and two old ones on ZDT crest. After rejecting them, and following Heyman (2014), we assign a class (A for well-, B for moderately- and C for poorly- clustered ages) to each moraine, using reduced Chi-square analyses (also see Chevalier and Replumaz, 2019). While the average age is taken to represent the most likely abandonment age of Class A moraines, the oldest age is instead taken for Classes B and C moraines (Heyman, 2014) because even though moraines are relatively stable landforms over the long term, crests are slowly adjusting following their abandonment, with boulders being gradually exhumed to the surface (hence their younger ages), thus representing multiple stages of exhumation as the surface lowers due to erosion of the matrix (e.g., Chevalier and Replumaz, 2019). Therefore, and because we assume zero erosion and did not correct for potential snow and vegetation cover, the apparent ages we calculate are minimum ages. Eventually, we assign a Marine oxygen Isotope Stage (MIS) (e.g., Lisiecki and Raymo, 2005) to each moraine which indicates the climatic period during which the moraine was abandoned.

4. Sites description and results

We describe the faults and study sites from NW to SE along the SE XSH fault (Fig. 2B). First, we introduce our preliminary results attesting to the central Yalahe fault activity, just north of Yala Mountain (Fig. 4), then describe the newly discovered 'Mugecuo South' fault zone (Fig. 5) located on the NE flank of the Zheduoshan Range between the Selaha and Zheduotang faults. We then present the two study sites, ZDT moraine along the Zheduotang fault (Figs. 6, 7) and MX moraine along the Moxi fault (Figs. 7, 8).

4.1. Yalahe fault

The Yalahe fault constitutes the NE branch of the right-stepping, en-echelon faults of the

active SE XSH fault (Fig. 2B). It runs from the eastern Huiyuansi basin where it strikes N108°E, cuts across the slopes of Taizhan valley and merges with the N141°E-striking Yalahe geologic fault along the northern side of Yala Mountain (peak at 5820 m), where it more or less follows the Yalahe valley for ~18 km until it reaches Kangding city (Fig. 2B,C). The Yalahe geologic fault extends ~130 km NW of Taizhan before merging with the XSH fault. Near Taizhan, the granitoids are affected by a ~1.3 km-wide zone of ductile and brittle deformation linked to the left-lateral Yalahe fault (Chen et al., 1985). The northern boundary of the Gongga-Zheduoshan batholith shows an apparent minimum offset of 15 km (AA' in Fig. 2C), but the offset of the southern boundary may be as large as 50 km (Bai et al., 2018) (AA'' and BB' in Fig. 2C).

The active NW part of the Yalahe fault bounds the SE Huiyuansi basin, which was created thanks to the significant oblique (left-lateral/normal) component of motion along that segment, in agreement with its oblique strike direction compared to that of the main XSH fault (e.g., Allen et al. 1991) (Fig. 2B). Aerial photograph analyses (Allen et al., 1991) and field investigation (Liang et al., 2020) show that the central part of the fault between ~Taizhan and Yala Mountain has a clear trace suggesting that it is also active. The fault can be followed for ~7 km on satellite images, and during our own field investigation, we found a ~1 m-high fault scarp along ~2.4 km of the fault (Fig. 4), i.e., a total of at least ~10 km, as recently reported by Liang et al. (2020), who also found several co-seismic (2.5-3.5 m) as well as one cumulative (~15 m) horizontal offsets along that central section. Just SE of Yala Mountain however, in the large U-shaped Yalahe valley (Fig. 4B), the fault trace cannot easily be followed on satellite images, either because this section may be inactive at present with activity having been transferred to the Selaha fault (e.g., Zhang et al., 2017; Bai et al., 2018), or because of the dense vegetation making remote sensing analyses difficult. Extra field work is clearly necessary to constrain the behavior of the Yalahe fault along its SE section. While Allen et al. (1991) found no evidence of the Yalahe fault closer to Kangding city, most likely due to the numerous villages in that valley hindering precise aerial mapping due to human modifications, Liang et al. (2020) reported it from cross-sections at a few locations (Fig. 2B), where they found

312 that the active Yalahe fault cuts through gravel strata underneath radiocarbon-dated, early to mid-
313 Holocene alluvial surfaces.

314

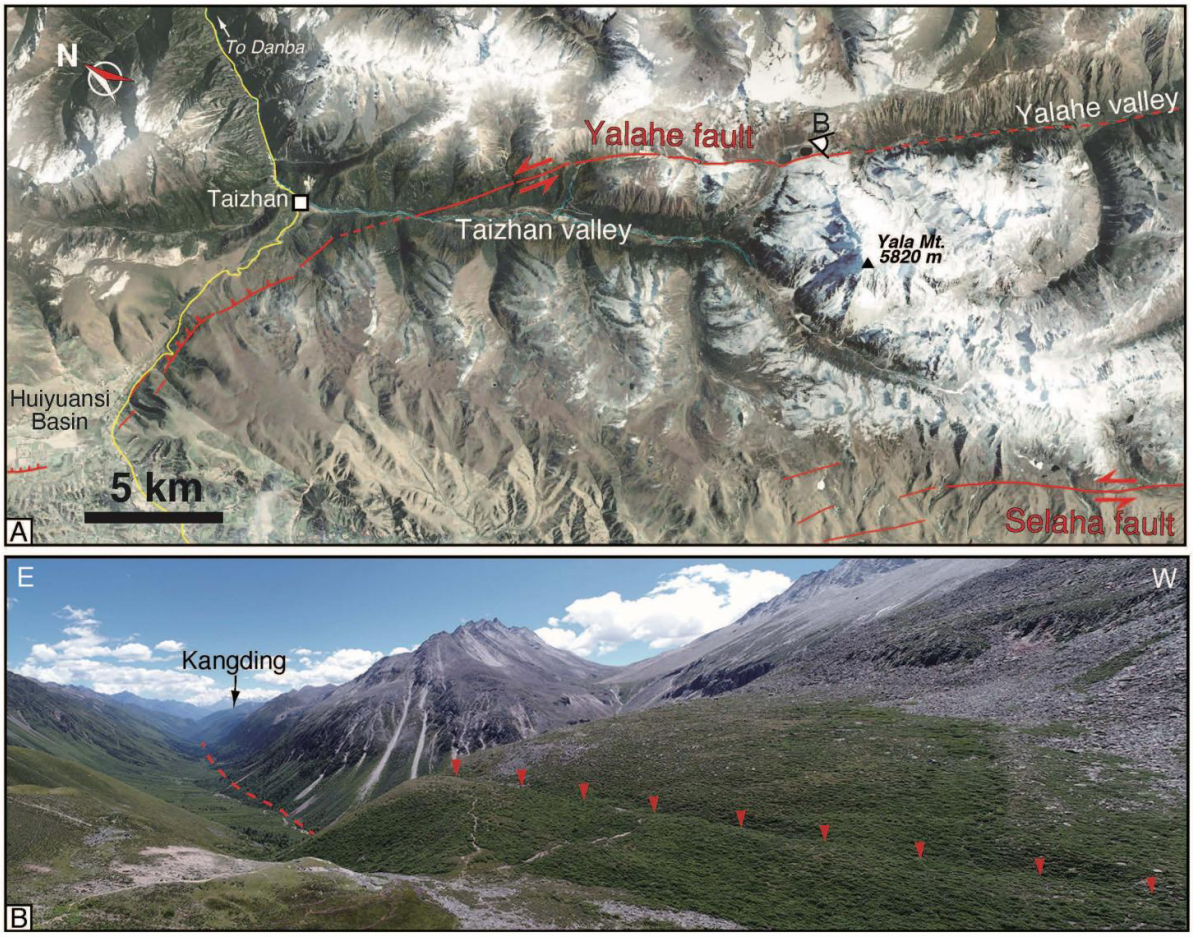

315

316 ***Figure 4:*** *Yalahe fault. (A) Google Earth image of Yalahe fault between Huiyuansi Basin and*
317 *Yalahe valley. Legend as in Figure 1. (B) View looking south along fault, with clear, linear, ~1 m-*
318 *high scarp. Farther SE, fault trace becomes hard to follow (dashed line).*

319

320 **4.2. Selaha fault and Mugecuo pull-apart**

321 While the Selaha fault was suggested as the main active branch of the SE XSH fault (Bai et
322 al., 2018), its trace between the Selaha pass and Mugecuo Lake is not as clear as that farther NW
323 and SE (Fig. 2B). To the NW, morphological evidence for active faulting abound along a linear

N144°E trend where the TG and SLH sites of Bai et al. (2018) are located (Fig. 2B), following the geological fault that separates the Gongga-Zheduoshan batholith from Triassic sediments (Chen et al., 1985) (Fig. 2C). It is along that fault that the Mw5.6 and Mw5.9 Kangding earthquakes occurred in 2014. These earthquakes exhibit purely strike-slip focal mechanisms with a nodal plane striking N139°-143°E for the first one and N148°-152°E for the second one (Jiang et al., 2015a), i.e., parallel to the NW Selaha fault (Fig. 2A). The fault left-laterally offsets the batholith's western edge by ~15 km (Roger et al., 1995; Bai et al., 2018) (CC' in Fig. 2C). To the SE, the fault is continuous and linear again, trending N154°, where Bai et al. (2018)'s YJG site is located (Fig. 5A). Between these two linear fault splays, the strike of the Selaha fault is however N116°E for ~14 km, where Mugecuo Lake is located. This segment probably has an important normal component and defines a releasing bend (Allen et al., 1991; Bai et al., 2018). However, the precise geometry and individual fault traces in that releasing bend were not clearly documented until now.

The ~600 m-high (Fig. 5F), steep topographic slope marking the north bank of Mugecuo Lake (Yala Range) most likely corresponds to the morphological expression of a recent normal fault trending N116°E and is cut by several topographic scarps that we interpret as secondary faults (Fig. 5A). South of the lake, the NE slopes of the Zheduoshan Range (NW part of Daxue Range) are less steep but our UAV (Fig. 5C) and field (Fig. 5B,D,E) surveys revealed countless ~N110°-140°E-trending topographic scarps up to ~10 m-high, in a ~22 km-long, ~3 km-wide, ~N120°E zone (Pan et al., 2020). We interpret these scarps as the morphological expression of active normal faults constituting the 'Mugecuo South fault zone' (Pan et al., 2020), which not only confirm that the Mugecuo Lake area is a releasing bend between the two linear splays of the Selaha fault, but also show that it is a 14x4.5 km-large pull-apart basin with Mugecuo Lake located at its lowest point (Figs. 2B and 5A,F).

While Wen (2000) and Wen et al. (2008) inferred, following Li et al. (1997), that the M7.0 1725 earthquake produced ~35 km of surface ruptures along the SE Selaha fault, with maximum co-

seismic offsets of ~3.5 m, we however, infer that this earthquake may have occurred on the Mugecuo South fault zone, which was unknown until now. This is partly due to the fresher nature of the scarps with free-faces (dip >70°, Fig. 5B) at places along the Mugecuo South fault zone, compared to those along the SE Selaha fault, although not as fresh as those from the 1955 earthquake that occurred along the Zheduotang fault.

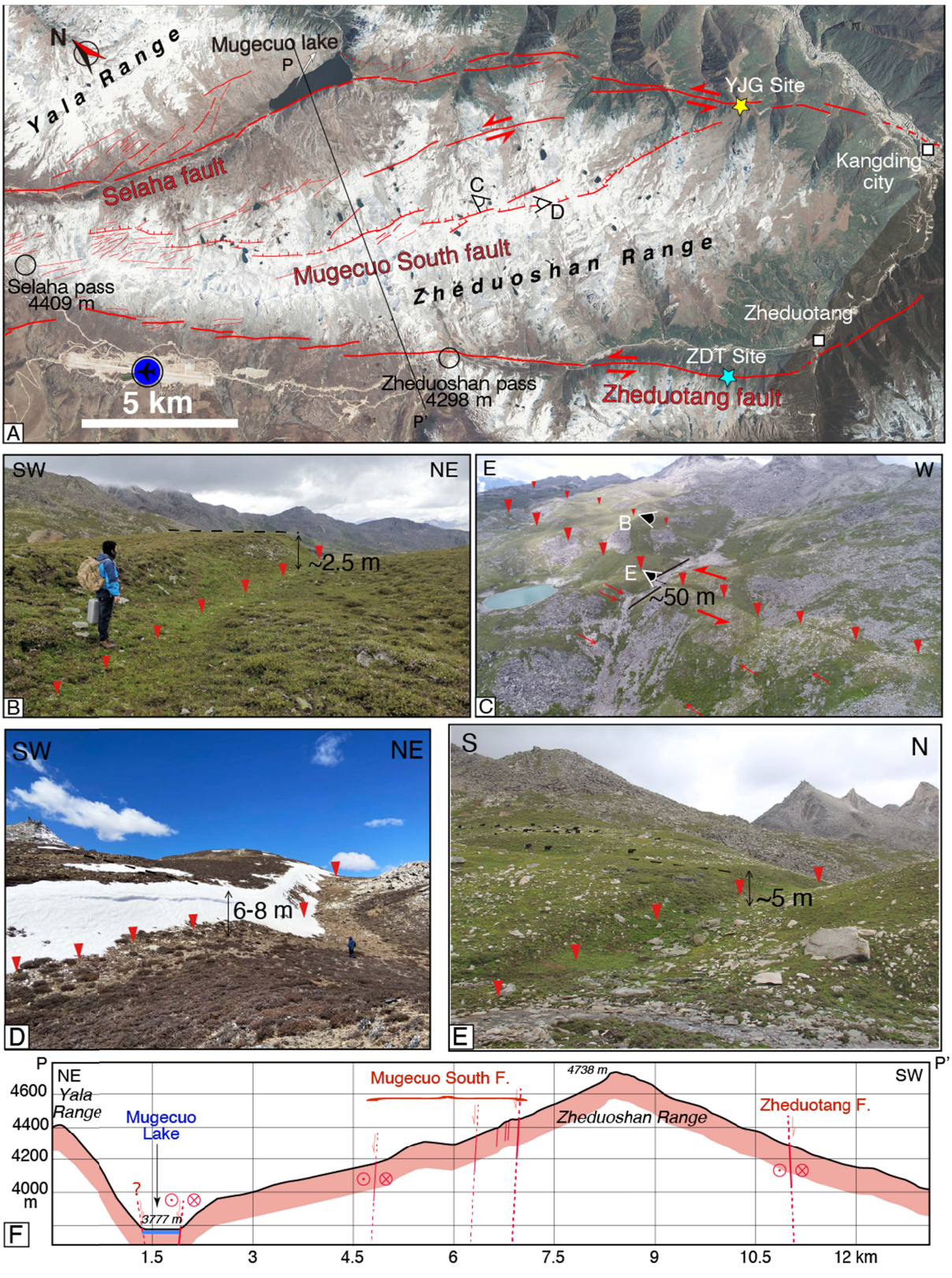

Figure 5: *Mugecuo South fault zone and releasing bend. (A) Google Earth image of Selaha, Zheduotang and Mugecuo South faults between Selaha pass and Kangding. Legend as in Figures 1 and 2. (B,D,E) Field photos of fault scarps along Mugecuo South fault zone. (C) UAV photo of*

faults from Mugecuo South fault zone highlighted by red triangles and arrows. Note left-lateral offset. (F) Topographic profile across Mugecuo pull-apart and Zheduoshan Range (NW part of Daxue Range). Recent faults in red, dashed where unknown.

4.3. Zheduotang fault and ZDT site

South of the Mugecuo pull-apart, the ~27 km-long, N148°-striking Zheduotang fault left-laterally offsets the western boundary of the Gongga-Zheduoshan batholith by ~10 km (Bai et al., 2018) (DD' in Fig. 2C). The fault follows the SW slopes of the Zheduoshan Range for ~13 km, from Kangding airport to the Zheduoshan pass, before becoming hard to follow in the valley due to the Kangding-Lhasa highway, until it reaches the mountain slopes on the other side of the valley (Fig. 5A). There, the Zheduotang fault sharply cuts about half-way for ~7 km, the NE-facing, steep (~35°), slopes on which numerous rockslides are present (Fig. 6A,B,D). It is along that section that the fault best displays left-lateral offsets of moraines (Fig. 6A,D). The fault has a slight normal component of motion with SW (uphill)-facing scarps, resulting in numerous sag ponds along the fault, particularly impressive along the section between the highway and Zheduotang village where the scarps can reach 8-10 m-high (Fig. 6B,C). That section ruptured during the 1955 Mw7.5 earthquake, that shows a purely left-lateral focal plane (N137°E, dip 89° to SW, obtained by recalibration of the initial motion directions of P waves recorded by 10 strong earthquakes along the XSH fault, Lin et al., 1986) that is roughly parallel to the fault trace (N148°E) (Fig. 2A). Farther to the SE, the Zheduotang fault changes direction to become ~N95°, reaches the valley again at Zheduotang village and cuts the mountain slopes for another ~2 km before it becomes hard to follow (Fig. 6A).

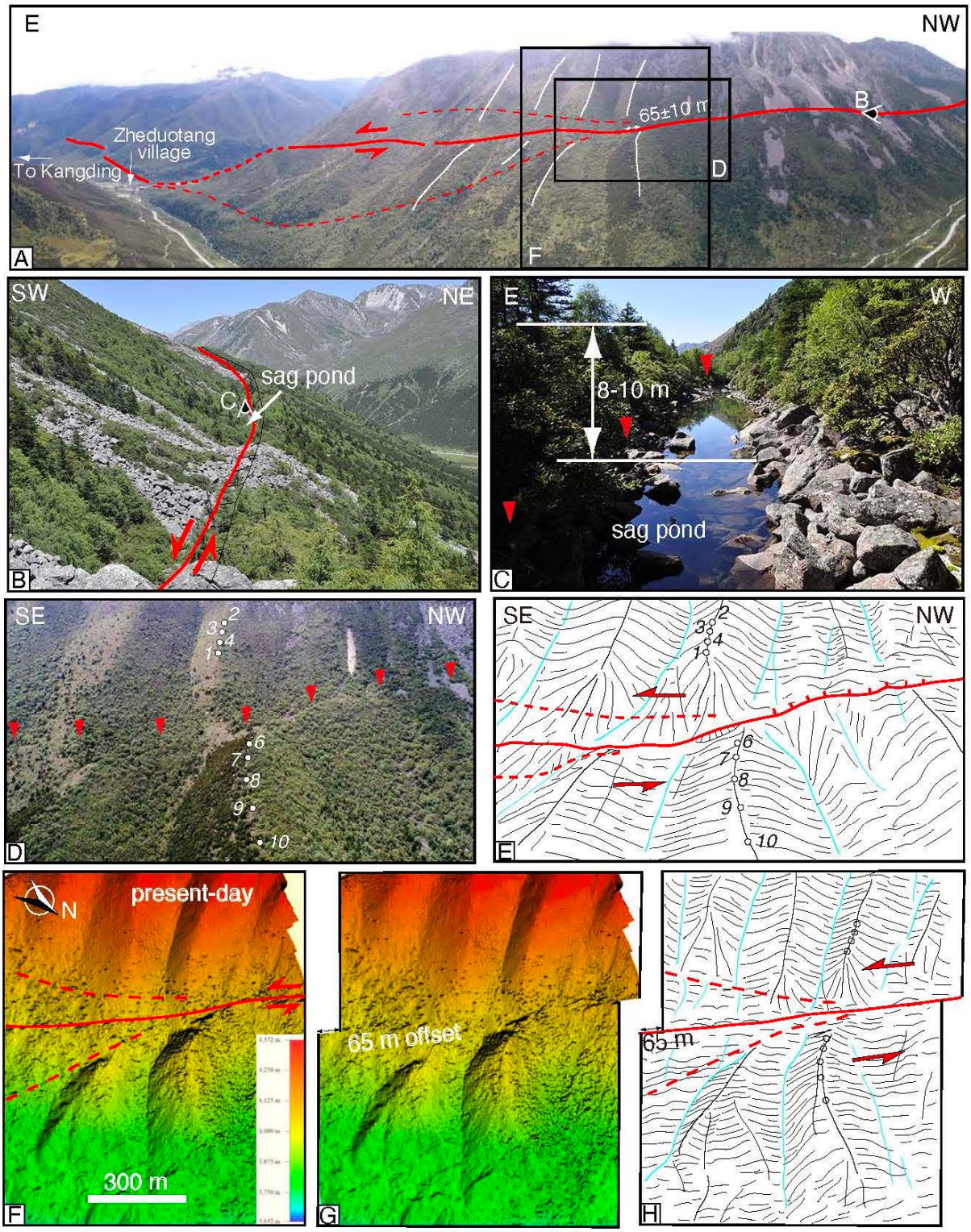

382

383 ***Figure 6:*** *Zheduotang fault and ZDT site. (A) Panoramic UAV photo of SE segment of Zheduotang*
384 *fault with white lines highlighting offset moraine crests. (B) Photo of uphill-facing fault scarp along*
385 *which numerous sag ponds are present. (C) Photo of uphill-facing, 8-10 m-high, fault scarp. (D,E)*
386 *UAV photo of ZDT moraine with white circles and numbers representing collected samples (ZDT-1*

to 10) and its interpretation. (F,G) Present-day and offset reconstruction of 65±10 m offset on LiDAR DEM obtained from our UAV surveys. (H) Interpretation of G.

The remote Zheduotang (ZDT) moraines are located ~ 10 km due west of the city of Kangding, at ~3860 m of elevation (Figs. 2B and 6). Their sub-rounded crests are ~1 km-long and are covered with medium-sized granite boulders (~1 m of diameter) (Fig. S1). While the upper crest is only covered with small bushes and occasional trees, the lower crest is covered with denser vegetation, especially on its outer slope (Fig. 6D). The Zheduotang fault cuts and left-laterally offsets the ZDT moraines by 65±10 m (Figs. 6F-H). The steep slopes, extremely dense vegetation at lower elevations, numerous rockslides with very large, angular boulders, and the large stream at the base of the mountain slopes (difficult to cross), all made this site extremely challenging to reach. We eventually were able to collect a total of nine samples from the NW crest: five upstream from the fault (ZDT-1-4) and five downstream (ZDT-6-10) (Fig. 6D). Ages range from 12.7±1.0 ka to 30.0±2.4 ka (Fig. 7 and Table 2). Applying statistical tests (see method section) allows to discard the two oldest samples, with the remaining seven samples being well-clustered (moraine is Class A), ranging from 12.7±1.0 to 15.9±1.2 ka. Therefore, the average age, 14.3±1.1 ka, is taken to represent the moraine's abandonment age. Combining offset and age yields a left-lateral slip-rate of 4.5(+0.9/-0.8) mm/yr, or a range of slip rate between 3.7 and 5.4 mm/yr.

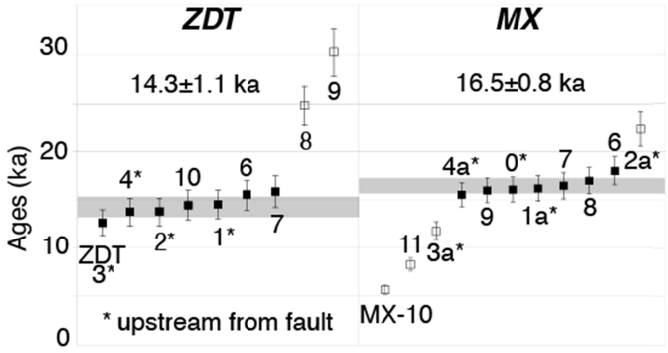

Figure 7: *^{10}Be cosmogenic surface-exposure ages of ZDT and MX moraines, calculated using CRONUS v3 (Balco et al., 2008), with 'Lm' production rate model (Lal (1991)/Stone (2000) time-dependent model). Outliers (open symbols) were discarded using Chauvenet and Peirce criteria (see method section for details).*

Table 2: *^{10}Be surface-exposure ages of Zheduotang (ZDT) and Moxi (MX) sites of the SE Xianshuihe fault.*

Sample name	Lat (°N)	Long (°E)	Elev.	shielding	10Be(at/g)	Lm ages (yrs)	Int. Uncert.	LSDn ages (yrs)	Int. Uncert.
ZDT site									
upstream ZDT-1	30.007218	101.853394	3938	0.97	582604±9527	**14523±1132**	241	14815±922	246
ZDT-2	30.007075	101.852399	4024	0.97	569669±11427	**13748±1083**	280	13920±881	283
ZDT-3	30.007142	101.85266	3998	0.97	506680±9258	**12655±990**	234	12908±808	239
ZDT-4	30.007173	101.853023	3954	0.97	544843±12160	**13643±1083**	309	13863±888	314
downstream ZDT-6	30.008677	101.855455	3818	0.97	588013±11776	**15418±1217**	314	15771±1000	321
ZDT-7	30.00863	101.855689	3813	0.97	604810±11605	**15863±1249**	310	16259±1027	318
ZDT-8#	30.008681	101.856037	3831	0.97	1018291±17250	**24910±1968**	434	25226±1591	439
ZDT-9#	30.009041	101.856574	3796	0.97	1222029±15333	**30046±2360**	389	30494±1901	395
ZDT-10	30.00918	101.856736	3779	0.97	534327±9037	**14453±1129**	248	14817±924	255
Moxi site									
upstream MX-0	29.88182	102.009519	3877	0.99	644968±14438	**16099±1282**	373	16434±1056	382
MX-1a	29.881898	102.009739	3879	0.99	651371±19511	**16231±1334**	504	16556±1115	516
MX-2a#	29.881799	102.00999	3879	0.99	941220±19057	**22354±1779**	472	22654±1448	479
MX-3a#	29.881875	102.01018	3868	0.99	448416±10022	**11810±936**	273	12148±777	281
MX-4a	29.881813	102.010269	3870	0.99	620232±14033	**15559±1240**	365	15905±1022	374
downstream MX-6	29.883161	102.011295	3865	0.99	726534±15952	**18029±1437**	411	18470±1186	421
MX-7	29.883558	102.010804	3887	0.99	666039±21318	**16481±1368**	548	16866±1153	560
MX-8	29.880397	102.011228	3881	0.99	686869±13617	**17022±1345**	350	17392±1103	358
MX-9	29.882661	102.012665	3862	0.99	636352±12761	**16002±1264**	333	16361±1038	340
MX-10#	29.882107	102.0135603	3838	0.99	196027±6791	**5748±478**	204	6031±415	214
MX-11#	29.879169	102.016253	3777	0.99	290547±8810	**8329±680**	260	8714±584	273

Samples were processed at the Institute of Crustal Dynamics, China Earthquake Administration, Beijing (now called National Institute of Natural Hazards, Ministry of Emergency Management of China), and the ^{10}Be/^{9}Be ratios were measured at GNS Science in New Zealand.

Ages are calculated with the CRONUS v3 calculator (Balco et al., 2008). Sample names with # represent outliers that

were statistically rejected (see text). All samples are granite (density 2.7 g/cm3); Shielding factor is 0.99 and 0.97 for Moxi and ZDT sites, respectively. Thickness is 5 cm.

No erosion rate was applied. Standard used at GNS is '01-5-4', with $^{10}Be/^{9}Be$ = 2.851e-12.

Lm=Lal (1991)/Stone (2000) time-dependent production rate model; LSDn=Lifton et al. (2014) production rate model.

4.4. Moxi fault and MX site

The NNW-striking Moxi fault runs from Kangding to Moxi cities (Fig. 2B,C), lying between the Proterozoic Kangding igneous complex and slivers of Paleozoic rocks (Lu et al., 1975; Liu et al. 1977). The fault shows evidence of recent faulting along its northern section where it cuts through the western slopes of the Lamo-She Range, crosses the Yajiageng (or Xuemenkan) pass (3830 m) then cuts through the eastern slopes of the Daxue Range (where Gongga Shan lies) (Fig. 8A). The fault is very clear, with numerous offset moraines, gullies, and alluvial fans, forming sag ponds at places thanks to its slight normal component of motion, with NE-facing scarps north of the pass and SW-facing scarps to the south. While the main Moxi fault lies quite low on the mountain slopes, numerous other fault strands are present higher on the slopes near the Yajiageng pass ('Moxi rupture' in Fig. 8A,B) (Yan et al., 2019), with W to SW-facing scarps damming sag ponds. Farther SE, the fault trace becomes harder to follow because it reaches the Moxi valley, which is filled with large streams (coming directly from Gongga Shan), huge fluvio-glacial terraces and rockslide deposits.

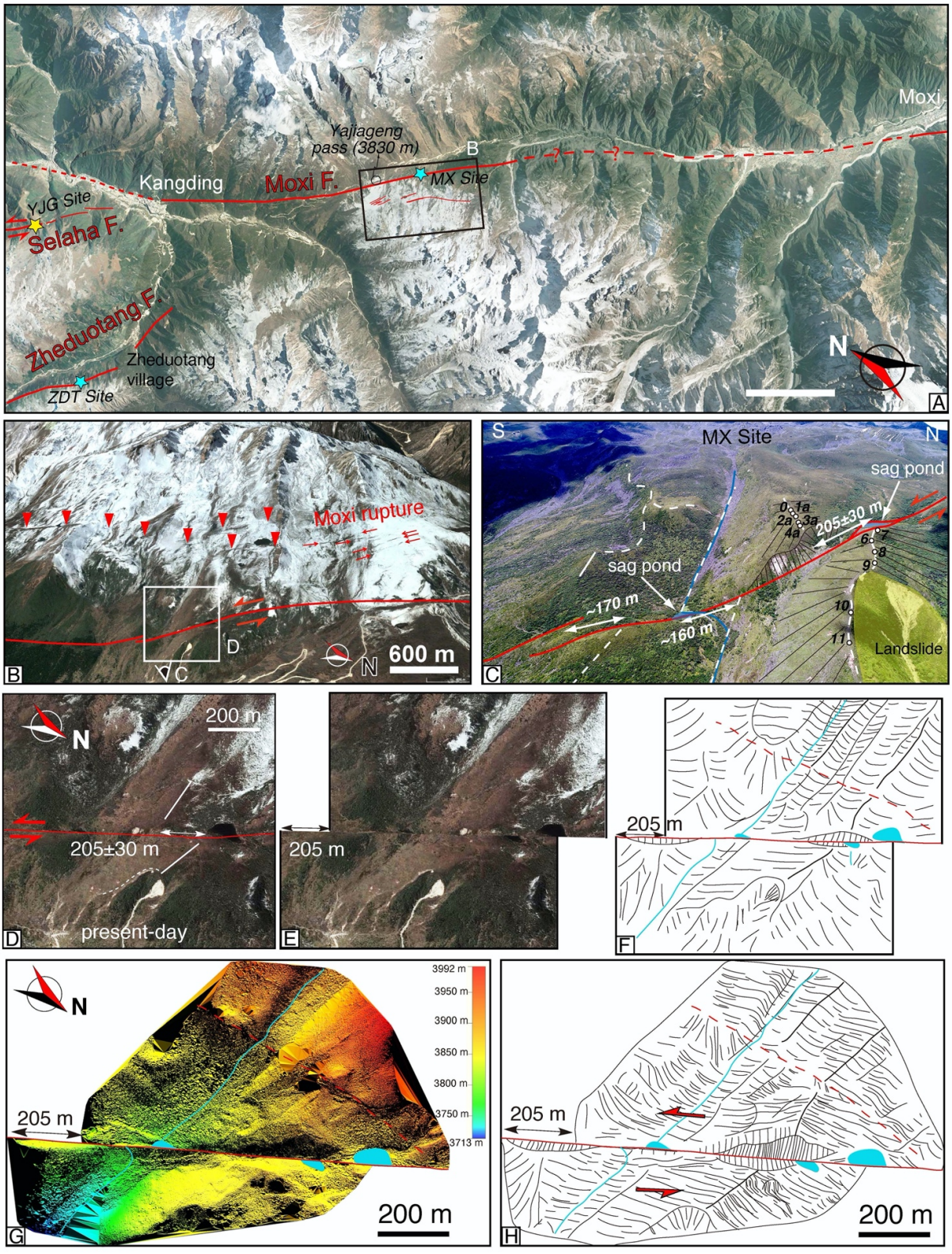

438

439 ***Figure 8:*** *Moxi fault and MX site. (A) Google Earth image of Moxi, SE Zheduotang and Selaha*
440 *faults. Legend as in Figures 1 and 2. (B) Google Earth 3D image of Moxi surface ruptures parallel*
441 *to Moxi fault, located ~1 km to the west. (C) UAV photo interpretation of MX moraine. (D,E)*

Present-day and offset reconstruction of the 205±30 m offset on Google Earth image. (F) Interpretation of E. (G) Offset reconstruction of the 205±30 m offset on LiDAR DEM obtained from our UAV and LiDAR surveys. (H) Interpretation of H.

The ~1.5 km-long Moxi (MX) moraines are located along the segment just SE of the Yajiageng pass, ~ 15 km SE of Kangding, at ~3850 m of elevation (Fig. 8). The MX moraine crests are sub-rounded and covered with small bushes, and with medium granite boulders (Fig. S2). A landslide removed part of the main moraine downstream from the fault (Fig. 8). Thanks to the left-lateral motion on the Moxi fault, two sag ponds at the base of the resulting SW-facing scarps formed, larger at the base of the northern crest (north of the stream, Fig. 8). The main northern and southern (i.e., south of the stream) MX moraine crests are left-laterally offset by 205±30 and ~170 m, respectively (Fig. 8). A smaller offset for the southern crest is excepted due to the sense of motion of the Moxi fault, with the stream in between, whose offset is ~160 m at present, constantly refreshing the lateral slopes.

We collected 11 samples at the MX site along the northern crests, five upstream from the fault (MX-0, MX-1a-4a) and six downstream (MX-6-11) (Fig. 8C). Ages range from 5.7±0.5 to 22.3±1.8 ka (Fig. 7 and Table 2). Applying statistical tests allows to discard the three youngest and the oldest samples. It is interesting to note that the young outliers are located the farthest downstream, most likely reflecting material removal due to the landslide, which has reshaped the crest to its present-day geometry. The original crest may thus only be preserved close to the fault, where samples MX-6 to 9 are located. The seven remaining samples cluster very well and the moraine is Class A. Therefore, the average age is taken to best represent the moraine's abandonment age, which is 16.5±0.8 ka. Combining the offset and the age of the main, northern moraine yields a left-lateral slip-rate of 12.5(+2.3/-2.1) mm/yr, or a range of 10.4 to 14.8 mm/yr. Note that the 'Moxi rupture' (located ~1 km west of the Moxi fault, Fig. 8B) may also absorb part of the deformation, thus the slip rate we determined is a minimum.

5. Discussion

5.1. Late Quaternary slip distribution across the various segments of the SE Xianshuihe fault

Along the NW XSH fault, where the single fault trace is linear and continuous, late Quaternary left-lateral slip rates have been estimated at 8 - 11 mm/yr (#13a, Fig. 3 and Table 1) (Zhang, 2013, reinterpreting Chen et al. (2008)'s data) and ~8.4 mm/yr (#14) (Liang et al., 2020). From the Huiyuansi Basin, where the XSH fault splits into the Yalahe, Selaha, Mugecuo South and Zheduotang branches, Bai et al. (2018), using the same technique as in this paper, determined rates of 9.6-9.9 (TG+SLH sites, Fig. 3B) and 3.9 - 4.9 mm/yr (YJG site) along the NW and SE parts of the Selaha fault, respectively, since ~20 ka. Our present study at the ZDT site allowed us to determine a late Quaternary (~15 ka) rate of 3.7 - 5.4 mm/yr along the Zheduotang fault. Summing the slip rates along the SE Selaha fault (YJG site) and the Zheduotang fault (ZDT site) yields 7.6-10.3 mm/yr (ZDT+YJG, Fig. 3). This appears to confirm the inference of Bai et al. (2018) that recent motion on the NW Selaha fault is then partitioned between the SE Selaha and the parallel Zheduotang faults farther to the SE. However, the total XSH fault slip rate at this longitude should also consider that along the Yalahe fault although it has been estimated to be quite low, and only from its NW part where its normal component is important (Figs. 2B and 4A). It was first qualitatively inferred as ~0.8 mm/yr (#12b, Fig. 3 and Table 1) (Allen et al., 1991), before being constrained at 1.8 - 2.2 mm/yr over 10 ka (#20a) (Zhou et al., 2001) and 0.6 (over 10-15 ka) - 1.5 (over 70 ka) mm/yr (#21a) (Chen et al., 2016) from thermoluminescence ages. Therefore, assuming similar rates along the SE Yalahe fault (0.6-2.2 mm/yr), in the absence of reported quantitative measurements, the total late Quaternary slip rate across the Yalahe, SE Selaha and Zheduotang branches becomes >8.2-12.5 mm/yr. Note that this rate is a minimum because the rate along the Mugecuo South fault is currently unknown.

Along the Moxi fault, we determined a slip rate of 10.4 - 14.8 mm/yr since ~16 ka at the MX

493 site. Previously published rates (Zhou et al., 2001; Chen et al., 2016; Yan et al., 2017) range from
494 8.3 to 10.5 mm/yr at the northern extremity of the fault (Fig. 3 and Table 1). These three studies
495 used ^{14}C dating mostly in trenches dug across the fault, a method that is not the most accurate for
496 determining slip rates along strike-slip faults because horizontal offsets are difficult to measure in
497 trenches. Considering that all measurements are valid and assuming a constant rate along the fault
498 would imply a rate of ~10.4 mm/yr along the entire Moxi fault.

499 From NW to SE, the late Quaternary slip rates along the XSH fault system thus appear to
500 increase progressively from ~6-8 mm/yr along the Ganzi fault (Chevalier et al., 2017), ~8 - 11
501 mm/yr along the single-stranded NW XSH fault (Zhang, 2013, Liang et al., 2020), >8.2-12.5 mm/yr
502 across the Yalahe / Selaha / Mugecuo / Zheduotang segment (e.g., Bai et al., 2018, this study), to
503 10.4-14.8 mm/yr along the Moxi segment (Figs. 3B,C and 9).

504

505 **5.2 Comparison with geodetic rates**

506 Comparison between our late Quaternary rates and geodetic ones is not straightforward, in
507 part due to the still limited number of regional GPS stations north of the XSH fault. The two latest
508 publications based on GPS data have adopted different strategies.

509 On one hand, Wang et al. (2020) propose an elastic block model (Meade and Loveless,
510 2009) for SE Tibet that explains well the ~15 years-long dataset (Wang et al., 2017), especially
511 north of the Red River fault. They further discuss the along- and across-strike slip rates of the faults
512 in their model. They infer a 11.8±0.6 mm/yr slip rate along the Ganzi fault, that increases to
513 14.5±0.9 mm/yr (#10b in Fig. 3 and Table 1) along the XSH fault. The late Quaternary rates that we
514 propose (6–8 mm/yr for the Ganzi fault and >8.2 - 12.5 mm/yr for the SE XSH fault) represent
515 ~70% of these rates. This difference may be explained by the fact that the block model considers
516 that all deformation between the blocks is absorbed along the bounding faults while in fact, a

517 fraction of the deformation may also be absorbed by other smaller structures within the blocks.

518 On the other hand, Wang and Shen (2020) propose a GPS-derived deformation field for most
519 of continental China based on a ~15 years-long dataset. They consider that in Tibet, including in the
520 XSH fault region, deformation is mostly continuous and cannot be described by the relative motion
521 of minimally-deformed blocks. In that case, deformation is instead quantified along velocity
522 profiles. In order to see a clear trend in the rate evolution on both sides of the fault, it is wise to
523 make wide (~100 km) and long (>300 km) transects perpendicular to the fault, however not
524 specifically targeted to the particular study of the XSH fault. Profiles from Wang and Shen (2020)
525 show a slight increase of velocity from ~11 mm/yr across the Yalahe/Selaha faults (section A-A' in
526 Fig. 9A,B, #24a in Fig. 3 and Table 1), to ~13 mm/yr across the Moxi fault (section B-B', #24b).
527 While the limit between their sections AA' and BB' falls near the Selaha pass, these GPS estimates
528 are still consistent with what we determined at the late Quaternary timescale across faults from both
529 sections.

530 The most recent GPS datasets, analyzed in two different ways, both suggest a progressive
531 increase toward the SE of the left-lateral slip rate along the XSH fault, as we document in this study
532 at a much longer timescale. Similarly, the most recent InSAR study (Qiao and Zhou, 2021) suggests
533 an increase from 8.1 - 11.1 mm/yr along the NW XSH fault (#7b in Fig. 3 and Table 1), to 8.8 - 16
534 mm/yr across the SE XSH fault (#7c), and 16.5 - 19.3 mm/yr along the Moxi fault (#7d). Note
535 however that the authors invoke possible overestimate of the latter due to unwrapping and local
536 atmospheric errors. A SE rate increase until at least Moxi would be in agreement with the observed
537 eastward projected rate decrease observed from GPS vectors relative to stable Eurasia located north
538 of the XSH fault system, from the Bayan Har block to the Longmenshan block, as well as from the
539 Longmenshan block to the Sichuan Basin (Fig. 9A).

540

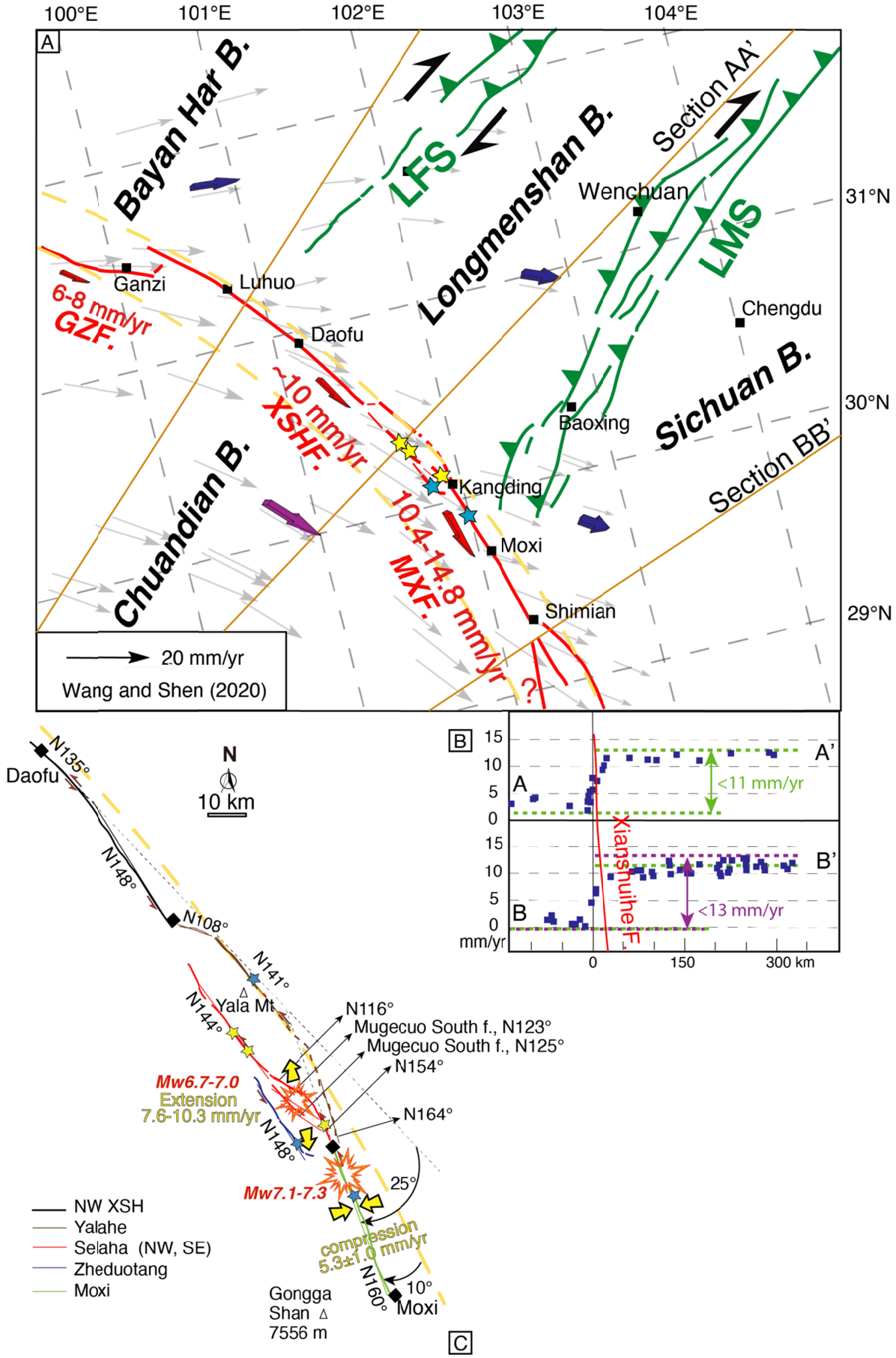
A
100°E
101°E
102°E
103°E
104°E
31°N
30°N
29°N
Bayan Har B.
LFS
Longmenshan B.
Section AA'
Wenchuan
LMS
Chengdu
Ganzi
Luhuo
6-8 mm/yr
GZF.
Daofu
~10 mm/yr
XSHF.
Baoxing
Sichuan B.
Chuandian B.
Kangding
Section BB'
10.4-14.8 mm/yr
MXF.
Moxi
Shimian
?
20 mm/yr
Wang and Shen (2020)
B
15
10
5
0
A'
A
<11 mm/yr
Xianshuihe F.
B'
B
<13 mm/yr
mm/yr
0
150
300 km
N
10 km
Daofu
N135°
N148°
N108°
N141°
Yala Mt
N144°
N116°
Mugecuo South f., N123°
Mugecuo South f., N125°
N154°
N164°
Mw6.7-7.0
Extension
7.6-10.3 mm/yr
N148°
Mw7.1-7.3
25°
compression
5.3±1.0 mm/yr
N160°
10°
Moxi
Gongga
Shan
7556 m
NW XSH
Yalahe
Selaha (NW, SE)
Zheduotang
Moxi
C

Figure 9: *(A) Conceptual 2D model of Xianshuihe fault following India–Asia collision (modified from Bai et al., 2018). Red arrows show southeastward slip rate increase, with rates from Chevalier et al. (2017) along the Ganzi fault (GZF), Bai et al. (2018) (yellow stars) along Xianshuihe/Selaha fault (XSHF), and this study along Moxi fault (MXF) (light blue stars). LFS=Longriba fault system, LMS=Longmenshan. Orange dashed lines show small circles (with pole of rotation in eastern Himalayan syntaxis) that fit with trace of Xianshuihe fault system. Grey arrows show GPS vectors relative to stable Eurasia (Wang and Shen, 2020) with oblique orange lines representing extent of their fan-shaped sections AA' and BB' shown in (B). Blue and pink arrows show block movement on each side of Xianshuihe fault system with their appropriate lengths according to GPS velocities. (B) Tangential (sinistral positive) components of GPS velocity profiles modified from Wang and Shen (2020) (with respect to Eurasia) with maximum rate across Xianshuihe and Moxi faults in green and pink, respectively. This is consistent with the increase in slip rate between the two fault segments we suggest with our late Quaternary rates. (C) Fault traces (thick colored lines) and strike directions (thin colored lines) of Xianshuihe fault. Dashed black lines show ~25°clockwise bend between NW XSH and Moxi fault segments. Yellow arrows represent directions of extension (Mugecuo pull-apart basin and compression (Moxi fault). Earthquake hazard (and their estimated magnitude in red) is indicated by large orange stars (see discussion in text).*

5.3 Example of a pull-apart basin within a restraining bend

While the NW XSH fault has a single, linear and continuous trace striking N135°E for ~180 km, its geometry changes dramatically near the Huiyuansi Basin (N148°E), where it splits into the four en-echelon faults discussed here (Yalahe-Selaha-Mugecuo-Zheduotang), before resuming as a single fault trace striking N160°E (Moxi segment) (Figs. 2 and 9C). This ~25° clockwise bend has been interpreted to have formed a restraining bend that would explain the very high elevations of the Yala (peak at 5820 m) and Daxue (Gongga Shan peak at 7556 m) Ranges (Allen et al., 1991; Burchfiel et al., 1995; Zhang et al., 2017). Zhang et al. (2017) interpreted the onset of rapid exhumation (at a rate of ~1.85 mm/yr) of the Yala Range at ~9 Ma, as corresponding to the restraining bend initiation, and thus, to the propagation of the XSH fault first along the Yalahe fault. They then interpreted the exhumation rate decrease at ~4 Ma in the Yala Range, as due to slip rate

571 decrease along the Yalahe fault, and further activation of the Selaha and Zheduotang faults. This
572 resulted in a southward shift in the restraining bend from the Yala to the Daxue Range, where the
573 highest peaks are now located.

574 This mountain range indeed shows the fastest present-day erosion rates in the entire eastern
575 margin of the Tibetan Plateau, between 1.0±0.4 and 7.6±2.5 mm/yr, derived from ^{10}Be
576 concentrations in river sand (Ouimet et al., 2009; Cook et al., 2018) (orange contour in Fig. 2C).
577 Cook et al. (2018) estimated that such very fast localized exhumation (at rates of ~3 mm/yr) lasts
578 since 3–4 Ma. While this timing is consistent with that proposed by Zhang et al. (2017) using
579 thermochronology dating, Cook et al. (2018) suggested that the geometry of the restraining bend
580 can only account for a fraction of the fast exhumation rate. Indeed, considering that motion is purely
581 strike-slip along the XSH fault, a ~12.5 mm/yr (or 10.4-14.8 mm/yr) of left-lateral slip along the
582 Moxi segment (this study) in a 25° restraining bend (angle between the XSH and Moxi segments)
583 would imply a 5.3±1.0 mm/yr compression across the Moxi segment in a planar geometry (Fig.
584 9C). Such compression may potentially explain the high exhumation rates in the Daxue Range
585 (Cook et al., 2018). However, the entire XSH fault system appears to follow a small circle
586 corresponding to a Euler rotation pole located in the Eastern Himalayan Syntaxis (25.0829°N -
587 93.5747°E in Bai et al., 2018, Fig. 10A; 25.65°N - 94.31°E in Cook et al., 2018). Considering that
588 small circle as representing a direction of pure strike-slip motion, the bend then becomes ~10° (Fig.
589 9C), which would imply only 2.2±0.4 mm/yr of compression across the Moxi fault, an amount too
590 small to solely explain the fast present-day exhumation rates in the Daxue Range (Cook et al.,
591 2018). Sixty kilometers to the south, the Moxi fault splits into the Anninghe and Daliangshan faults
592 that left-laterally offset the Yangtze River by ~60 km (Wang et al., 1998) (near ~27°N, Fig. 1). The
593 northern Anninghe fault striking N185°E implies another ~25° of clockwise rotation of the direction
594 of motion, hence another restraining bend (Fig. 1). However, that bend is located too far south to
595 explain the high erosion and very high elevations in the Gongga Shan region (Cook et al., 2018).

Therefore, in this tectonic setting, subsidence in the Mugecuo area (Fig. 5A) is rather surprising in a zone of high elevations and recent fast exhumation rates. The geometry of the SE Selaha and Zheduotang faults is typical of a large-scale (~4.5 km-wide) pull-apart basin (Fig. 5A) in between the Yala Range, where fast exhumation occurred between 9 and 4 Ma (Zhang et al., 2017), and the Daxue Range, where very fast exhumation occurs since ~4 Ma (Cook et al., 2018). Local subsidence thus appears to be the consequence of strike-slip motion on the SE Selaha fault striking N154° and the Zheduotang fault striking N148° (Figs. 9C and 10). The corresponding amount of NW-SE extension within the Mugecuo pull-apart basin can thus be estimated by summing the rates along these two bounding faults: 3.9 – 4.9 mm/yr for the SE Selaha fault at the YJG site (Bai et al., 2018) and 3.7 - 5.4 mm/yr for the Zheduotang fault at the ZDT site (this study), thus a total of 7.6 – 10.3 mm/yr (Figs. 9C and 10). This value would correspond to that of the subsidence in the pull-apart basin if every fault strand was vertical, and would thus yield an upper bound for the total vertical motion.

At such rate, the ~600 m-deep Mugecuo Lake depression (Fig. 5F) would form in 60 to 80 kyrs. This only represents a first order estimate as it does not account for erosion nor the actual dip of the faults (which remains to be constrained). While these variables would both increase the pull-apart's duration of formation, it is nevertheless compatible with the ages of the regional offset landforms (e.g., Chevalier and Replumaz, 2019). In addition, in the pull-apart basin, vertical motion appears asymmetrical, with a ~300 m higher topography and more numerous normal fault strands on the SW side compared to that on the NE (Fig. 5F). This is consistent with much faster exhumation rates (determined from cosmogenic ^{10}Be basin-wide measurements) to the SW compared to the NE (Fig. 2C) (Ouimet et al., 2009; Cook et al., 2018). However, the zone of fastest exhumation is located ~30 km farther south (Cook et al., 2018) (Fig. 2C) and cannot be explained by the pull-apart kinematics alone. We thus interpret the Mugecuo zone as a pull-apart basin within a larger restraining bend (see discussion above), which implies a complex 3D fault geometry (Fig. 10) that has, to our knowledge, rarely been described.

A striking peculiarity of the Yalahe-Selaha-Mugecuo-Zheduotang segments is that they are located where the XSH fault crosscuts a ~120 km-long granite batholith that formed during at least four distinct magmatic episodes (obtained from U/Pb zircon ages): Triassic (Gongga granite, 216-204 Ma), Middle Jurassic (Zheduo granite, ~170 Ma), Oligocene (~27 Ma) and Miocene (20-13 Ma) (Roger at al., 1995; Li and Zhang, 2013; Li et al., 2015; Searle et al., 2016). This batholith is the only Cenozoic massif in all of SE Tibet, and crystallization ages as young as ~5 Ma have been reported (Searle et al., 2016; Zhang et al., 2017). Ar/Ar ages are as young as 3.5 Ma (Wallis et al., 2003; Zhang et al., 2004; Chen et al., 2006) and apatite fission track ages are as young as 1.2 Ma (Xu and Kamp, 2000; Wilson et al., 2011; Zhang et al., 2017). Such very young ages imply a high geothermal gradient that may be one of the contributing factors to the present-day fast exhumation rates (Cook et al., 2018). Indeed, young magmatism and high heat flow may favor uplift. However, young (≤5 Ma) granite bodies are rare and small in extent, so that it is challenging to quantify this possible effect.

It is also surprising that the local trace of the faults at the surface is so complex where it crosses the granite batholith, which is most likely more rigid than the surrounding Triassic flysh. Indeed, farther north, where the Ganzi segment of the XSH fault system cuts and offsets the Mesozoic Queer Shan granite by 76–90 km (Wang and Burchfiel, 2000; Wang et al., 2009), the fault trace is linear and does not appear to be affected by lithology (Fig. 1). Therefore, the key point may thus be that the young age of the granite and/or the high regional flow concur to create the high elevation of Gongga Shan, in addition to the precipitation that possibly pre-existed along the SE Tibetan Plateau margin due to the topographic step (Cook et al., 2018).

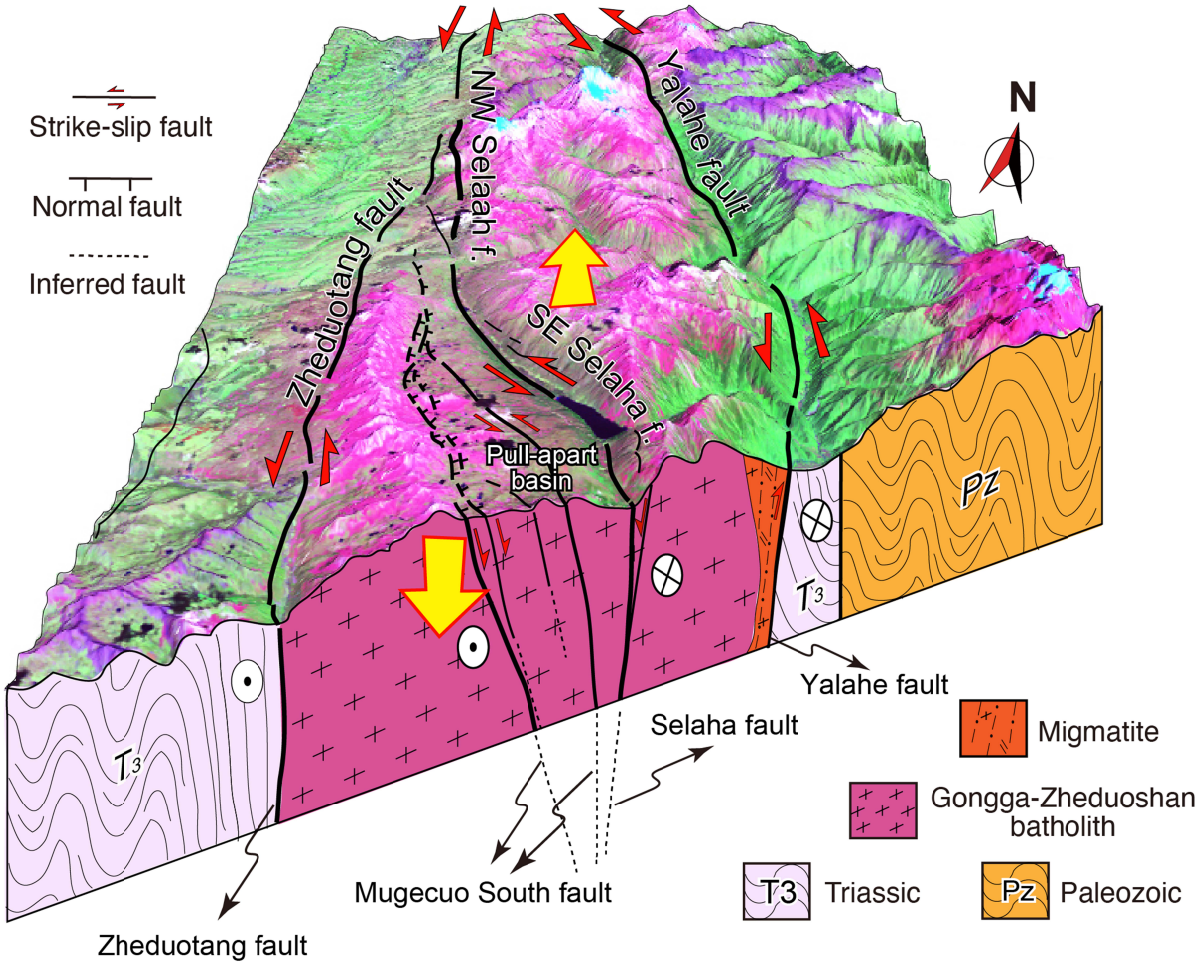

644

645 ***Figure 10****: 3D geomorphic model of Mugecuo South fault zone area (mostly normal, with minor*
646 *left-lateral motion), which forms a large-scale pull-apart basin with Mugecuo Lake in its lowest*
647 *point. Legend as in Figure 2. Top image is Landsat.*

648

649 **5.4 Seismic hazard in the Kangding region**

650 Using the late Quaternary slip rates we determined in this study helps us calculate the
651 current slip deficit since the last large earthquake occurred along a particular fault segment using
652 empirical equations from Wells and Coppersmith (1994). Satellite images analysis and field
653 investigation confirmed that at least the NW and central segments of the Yalahe fault are active with
654 recent, as well as cumulative, offsets, while the potential activity along the SE part remains to be
655 assessed. Taking a 0.6 - 2.2 mm/yr rate (as suggested for the NW part), a slip deficit of only 19 - 70

cm would have accumulated since the last large earthquake in 1700 (M7). This would correspond to a Mw6.2 - 6.6 earthquake hazard at present (Wells and Coppersmith, 1994: M=6.69+0.74*log[maximum displacement of 0.19 - 0.7 m]).

The Kangding region of the SE XSH fault is regarded as a seismic gap, partly because of the regional Coulomb stress increase following the 2008 Wenchuan (e.g., Parsons et al., 2008; Toda et al., 2008; Shan et al., 2009; Nalbant and McCloskey, 2011) and 2013 Lushan (Ms7.0) (Shan et al., 2013; Yang et al., 2015; Guo et al., 2018) earthquakes, and in part because the energy accumulated in the region since the 1955 Mw7.5 Kangding earthquake was only partly released during the 2014 Mw5.9 and 5.6 Kangding earthquake sequence (e.g., Jiang et al., 2015a; Xie et al., 2017). Based on the coulomb stress evolution of co-seismic dislocation and post-seismic viscoelastic relaxation, and on time-dependent probabilistic risk models, the Bamei-Selaha-Kangding segments in particular have been shown to have a high earthquake probability in the near future (e.g., Xu et al., 2013, 2019; Shao et al., 2016). Geophysical studies also indicate a high seismic hazard in that region (e.g., Jiang et al., 2015a; Wang and Shen, 2020).

At a more detailed level, the Selaha fault has especially been suggested as a seismic gap because of the absence of large earthquakes since 1748 along its NW section, and 1725 along its SE section, respectively, with a M~7 earthquake risk at present (e.g., Allen et al., 1991; Wen, 2000; Wen et al., 2008; Papadimitriou et al., 2004; Cheng et al., 2011; Shao et al., 2016; Bai et al., 2018; Qiao and Zhou, 2021). However, our discovery of the Mugecuo South fault zone followed by our recent field investigation, revealed numerous normal fault strands with cumulative fault scarps up to ~10 m-high at places (Pan et al., 2020). Although the geometry of the fault is different from that of the more linear and continuous traces of the Yalahe and Zheduotang faults, the numerous fault strands at the surface may connect at depth. Because the Selaha and Mugecuo South faults together form a large-scale pull-apart basin bounded by numerous normal fault strands, the pull-apart may lose stability more easily and rupture through (Segall and Pollard, 1980; Li et al., 2015). We thus

suggest that large earthquakes may more easily occur in that zone of the Mugecuo pull-apart basin, compared to other sections of the Selaha fault. As the slip rate along the Mugecuo South fault is still unknown, taking that of the NW or SE Selaha fault (~9.75 and 3.9 - 4.9 mm/yr, respectively), would yield a slip deficit of ~2.8 or 1.2-1.5 m, respectively since 1725. This would correspond to a potential earthquake as high as ~Mw6.7 - 7.0 at present (M=6.69+0.74*log[maximum displacement of 2.8 m], Wells and Coppersmith, 1994).

Similarly, taking our 10.4 - 14.8 mm/yr rate along the Moxi fault would correspond to a slip deficit of 2.4 - 3.5 m since the last large (M7.75) earthquake in 1786, i.e., a potential earthquake of Mw7.1-7.3 at present, consistent with what Qiao and Zhou (2021) determined (Mw7.37) using an elastic dislocation model. These authors also determined that the return time of characteristic large earthquakes (Mw7.25) along the Moxi fault is 155 years. The fact that the last large earthquake occurred 235 years ago may thus suggest that an earthquake is overdue along that segment hence a high seismic risk. This would devastate Moxi town, which, despite currently being less populated than Kangding city, continuously expands to cater to increasing tourism, thanks to its location at the base of Gongga Shan.

6. Conclusion

By studying four locations along the four en-echelon faults of the SE Xianshuihe fault:

(1) We quantitatively determined that the late Quaternary slip rate along the Zheduotang fault is 3.7 - 5.4 mm/yr.

(2) We discovered a new fault zone (Mugecuo South) between the SE Selaha and Zheduotang faults, along which numerous, mostly normal, fault strands with cumulative scarps up to ~10 m exist. Due to the fresh nature of the scarps, we infer that the 1725 M7.0 earthquake may have occurred along that particular fault zone. This new fault segment forms a large-scale pull-apart

basin causing subsidence of the Mugecuo Lake zone.

(3) The Mugecuo pull-apart basin is located in a zone of exceptionally high elevation (visible as highest peak Gongga Shan, 7556 m) due to the large-scale restraining bend along the Xianshuihe fault, possibly in conjunction with high heat flow and intense erosion.

(4) We suggest from field investigation, that the central part of the Yalahe fault is active, with clear fault scarps that can be followed for ~10 km. While slip rates are still lacking, we suggest that it most likely also contributes to the total slip rate of the SE Xianshuihe fault.

(5) We determined that SE of Kangding, the late Quaternary slip rate along the Moxi fault ranges from 10.4 to 14.8 mm/yr.

(6) The slip rate along the Xianshuihe fault system thus increases to the SE from 6-8 mm/yr along the Ganzi fault, to 8-11 mm/yr along the NW Xianshuihe fault, to 8.2-12.5 mm/yr along the SE Xianshuihe fault, to 10.4-14.8 mm/yr along the Moxi fault.

(7) We suggest that high seismic hazard exists in the SE Xianshuihe fault, especially in the Mugecuo pull-apart basin, which may facilitate earthquakes nucleation.

Acknowledgments

This work was financially supported by the National Natural Science Foundation of China [NSFC 42020104007, 41941016, 4191101281, 41672210], the China Geological Survey [DD20190059], the Key Special Project for Introduced Talents Team of Southern Marine Science and Engineering Guangdong Laboratory (Guangzhou) (GML2019ZD0201), and the Basic Outlay of Scientific Research Work from the Institute of Geology, CAGS [JYYWF20182104]. All geochronology data are in Table 2 and can be downloaded online (https://zenodo.org/record/5108951#.YPDufy0RrjA).

728 **References**

729 Allen, C.R., Luo, Z., Qian, H., Wen X., Zhou, H., & Huang, W. (1991). Field study of a highly
730 active fault zone: The XSF of southwestern China. *Geological Society of America Bulletin,*
731 *103*, 1178–1199. Doi:10.1130/0016-7606(1991)103<1178:FSOAHA>2.3.CO;2

732 Bai, M., Chevalier, M.L., Pan, J., Replumaz, A., Leloup, P.H., Métois, M., & Li, H. (2018).
733 Southeastward increase of the late Quaternary slip-rate of the Xianshuihe fault, eastern Tibet.
734 Geodynamic and seismic hazard implications. *Earth and Planetary Science Letters, 485,* 19-
735 31. Doi:10.1016/j.epsl.2017.12.045

736 Balco, G., Stone, J.O., Lifton, N. A., & Dunai, T.J. (2008). A complete and easily accessible means
737 of calculating surface exposure ages or erosion rates from ^{10}Be and ^{26}Al measurements.
738 *Quaternary Geochronology, 3*, 174-195. Doi:10.1016/j.quageo.2007.12.001

739 Bevington, P.R., & Robinson, D.K. (2002). Data reduction and error analysis for the physical
740 sciences. 336pp, McGraw-Hill

741 Burchfiel, B.C., Chen, Z., Liu, Y., & Royden, L.H. (1995). Tectonics of the Longmen Shan and
742 adjacent regions. *International Geology Review, 37*, 661–736

743 Chen, W., Tan, Q., Wen, P., & Liang, X. (1985). Geological map of Kangding (H-47-18). Sichuan
744 Institute of Geology and Mineral Resources, Scale 1/200,000

745 Chen, W., Zhang, Y., Zhang, Y.Q., Jin, G.S., & Wang, Q.L. (2006). Late Cenozoic episodic uplifting
746 in southeastern part of the Tibetan plateau-evidence from Ar–Ar thermochronology. *Acta*
747 *Geologica Sinica, 22,* 867–872. Doi:10.3969/j.issn.1000-0569.2006.04.010 (in Chinese)

748 Chen, G., Xu, X., Wen, X., & Wang, Y. (2008). Kinematical transformation and slip partitioning of
749 northern to eastern active boundary belt of Sichuan-Yunnan block. *Seismology and Geology,*
750 *30*, 58-85 (in Chinese)

751 Chen, G., Xu, X., Wen, X., & Chen, Y. (2016). Late Quaternary slip-rates and slip-partitioning on
752 the southeastern Xianshuihe fault system, Eastern Tibetan Plateau. *Acta Geologica Sinica, 90*,
753 537-554. Doi:10.1111/1755-6724.12689

754 Cheng, J., Liu, J., Gan, W., Yu, H., & Li, G. (2011). Characteristics of strong earthquake evolution
755 around the eastern boundary faults of the Sichuan-Yunnan rhombic block. *Science China–*
756 *Earth Sciences, 54*, 1716–1729. Doi:10.1007/s11430-011-4290-2

757 Chevalier, M.L., Ryerson, F.J., Tapponnier, P., Finkel, R., Van der Woerd, J., Li, H., & Liu, Q.
758 (2005). Slip-rate measurements on the Karakorum fault may imply secular variations in fault
759 motion. *Science, 307(5708)*, 411–414. Doi: 10.1126/science.1105466

760 Chevalier, M.L., Hilley, G., Tapponnier, P., Van Der Woerd, J., Liu-Zeng, J., Finkel, R.C., Ryerson,
761 F.J., Li, H., & Liu, X. (2011). Constraints on the late Quaternary glaciations in Tibet from
762 cosmogenic exposure ages of moraine surfaces. *Quaternary Science Reviews, 30*, 528–554.
763 Doi:10.1016/j.quascirev.2010.11.005

764 Chevalier, M.L., Leloup, P.H., Replumaz, A., Pan, J., Metois, M., & Li, H. (2017). Temporally
765 constant slip-rate along the Ganzi fault, NW Xianshuihe fault system, eastern Tibet.
766 *Geological Society of America Bulletin, 130(3/4),* 396–410. Doi:10.1130/B31691.1

767 Chevalier, M. L., & Replumaz, A. (2019). Bimodal climatic signal for glaciations in SE Tibet:
768 Marine Isotope Stages 2 and 6. *Earth and Planetary Science Letters, 507*, 105-118.
769 Doi:10.1016/j.epsl.2018.11.033

770 CEA: China Earthquake Administration, Earthquake Disaster Prevention Department. Catalogue of
771 strong earthquakes in Chinese history. *Beijing Seismological Press*, 1995.

772 Cook, K.L., Hovius, N., Wittmann, H., Heimsath, A.M., & Lee, Y. (2018). Causes of rapid uplift
773 and exceptional topography of Gongga Shan on the eastern margin of the Tibetan Plateau.
774 *Earth and Planetary Science Letters, 481,* 328–337, doi: 10.1016/j.epsl.2017.10.043
775 Dai, F.C, Lee, C.F., Deng, J.H., & Tham, L.G. (2005). The 1786 earthquake-triggered landslide dam
776 and subsequent dam-break flood on the Dadu River, southwestern China. *Geomorphology, 65,*
777 205–221. Doi:10.1016/j.geomorph.2005.06.011

778 Deng, Q., Zhang, P., Ran, Y., Yang, X., Min, W., & Chu, Q. (2003). Basic characteristics of active
779 tectonics of China. *Science in China, 46*, 356–372. Doi:10.1360/03yd9032

780 Friedrich, A.M., Wernicke, B.P., Niemi, N.A., Bennett, R.A., & Davis, J.L. (2003). Comparison of
781 geodetic and geologic data from the Wasatch region, Utah, and implications for the spectral
782 character of Earth deformation at periods of 10 to 10 million years. *Journal of Geophysical*
783 *Research, 108(B4)*, 2199. Doi:10.1029/2001JB000682

784 Gan, W., Zhang, P., Shen, Z., Niu, Z., Wang, M., Wan, Y., Zhou, D., & Cheng, J. (2007). Present-
785 day crustal motion within the Tibetan Plateau inferred from GPS measurements. *Journal of*
786 *Geophysical Research, 112*, B08416. Doi:10.1029/2005JB004120

787 Gosse, J., & Phillips, F. (2001). Terrestrial in situ cosmogenic nuclides: Theory and application.
788 *Quaternary Science Reviews, 20,* 475–1560. Doi:10.1016/S0277-3791(00)00171-2

789 Guo, R., Zheng, Y., Tian, W., Xu, J., & Zhang, W. (2018). Locking Status and Earthquake Potential
790 Hazard along the Middle-South Xianshuihe Fault. *Remote sensing, 10,* 2048.
791 doi:10.3390/rs10122048

792 Hallet, B., & Putkonen, J. (1994). Surface dating of dynamic landforms: young boulders on aging
793 moraines. *Science, 265*, 937-940. Doi: 10.1126/science.265.5174.937

794 Han, S., Li, H., Pan, J., Lu, H., Zheng, Y., Liu, D., & Ge, C., (2019). Co-seismic surface ruptures

795 in Qiangtang Terrane: Insight into Late Cenozoic deformation of central Tibet.
796 *Tectonophysics, 750*, 359–378. Doi :10.11016/j.tecto.2018.11.001

797 Heyman, J., Stroeven, A.P., Harbor, J., & Caffee, M.W. (2011). Too young or too old: Evaluating
798 cosmogenic exposure dating based on an analysis of compiled boulder exposure ages. *Earth*
799 *and Planetary Science Letters, 302,* 71–80. Doi:10.1016/j.epsl.2010.11.040

800 Heyman, J. (2014). Paleoglaciation of the Tibetan Plateau and surrounding mountains based on
801 exposure ages and ELA depression estimates. *Quaternary Science Reviews, 91*, 30–41.
802 Doi:10.1016/j.quascirev.2014.03.018

803 Ji, L., Zhang, W., Liu, C., Zhu, L., Xu, J., & Xu, X. (2020). Characterizing interseismic deformation
804 of the Xianshuihe fault, eastern Tibetan Plateau, using Sentinel-1 SAR images. *Advances in*
805 *Space Research, 66,* 378–394. Doi:10.1016/j.asr.2020.03.043

806 Jiang, G., Wen, Y., Liu, Y., Xu, X., Fang, L., Chen, G., Meng, G., & Xu, C. (2015a). Joint analysis
807 of the 2014 Kangding, southwest China, earthquake sequence with seismicity relocation and
808 InSAR inversion. *Geophysical Research Letters, 42,* 3273-3281. Doi:10.1002/2015GL063750

809 Jiang, G., Xu, X., Chen, G., Liu, Y., Fukahata, Y., Wang, H., Yu, G., Tan, X., & Xu, C. (2015b).
810 Geodetic imaging of potential seismogenic asperities on the Xianshuihe-Anninghe-Zemuhe
811 fault system, southwest China, with a new 3-D viscoelastic interseismic coupling model.
812 *Journal of Geophysical Research - Solid Earth, 120,* 1855–1873. Doi:10.1002/2014JB011492

813 Kohl, C.P., & Nishiizumi, K. (1992). Chemical isolation of quartz for measurement of in-situ -
814 produced cosmogenic nuclides. *Geochimica et Cosmochimica Acta, 56*, 3583-3587.
815 Doi:10.1016/0016-7037(92)90401-4

816 Lal, D. (1991). Cosmic-ray labeling of erosion surfaces-In situ nuclide production rates and erosion
817 models. *Earth and Planetary Science Letters, 104 (2-4)*, 424–439. Doi:10.1016/0012-

821X(91)90220-C

Li, Y., & Bürgmann, R. (2021). Partial coupling and earthquake potential along the Xianshuihe Fault, China. *Journal of Geophysical Research*, doi:10.1029/2020JB021406

Li, T., Du, Q., Zhang, C., & You, Z., 1997. The Active Xianshuihe Fault Zone and its Seismic Risk Assessment. Chengdu Cartographic Publishing House, Chengdu, 230 pp. (in Chinese)

Li, H., & Zhang, Y. (2013). Zircon U–Pb geochronology of the Konggar granitoid and migmatite: constraints on the Oligo-Miocene tectono-thermal evolution of the Xianshuihe fault zone, East Tibet. *Tectonophysics, 606,* 127–139. Doi:10.1016/j.tecto.2013.07.007

Li, Z., Xiao, H., & Zhou, B. (2015). Effect of fault steps on propagation and termination behavior of strike-slip earthquake surface rupture. *Seismology and Geology, 37(1),* 126-138 (in Chinese)

Li, T., Zhu, Y., Yang, Y., Xu, Y., An, Y., Zhang, Y., Feng, S., Huai, Y., & Yang, J. (2019). The current slip rate of the Xianshuihe fualt zone calculated using mutiple observation data of crustal deformation. *Chinese Journal of Geophysics, 62(4),* 1323-1335 (in Chinese)

Li J., Zhou, B., Li, T., Yang, Y., & Li, Z. (2020). Locking depth, slip rate, and seismicity distribution along the Daofu–Kangding segment of the Xianshuihe fault system, eastern Tibetan Plateau. *Journal of Asian Earth Sciences, 193,* 104328. Doi:10.1016/j.jseaes.2020.104328

Liang, M., Chen, L., Ran, Y., Li, Y., Wang, D., Gao, S., Han, M., & Zeng, D. (2020). Late Quaternary activity of the Yalahe fault of the Xianshuihe fault zone, eastern margin of the Tibet Plateau. *Seismology and Geology, 42(2),* 513-525. doi:10.3969/j.issn.0253-4967.2020.02.016 (in Chinese)

Lifton, N., Sato, T., & Dunai, T.J. (2014). Scaling in situ cosmogenic nuclide production rates using

analytical approximations to atmospheric cosmic-ray fluxes. *Earth and Planetary Science Letters, 386,* 149-160. Doi:10.1016/j.epsl.2013.10.052.

Lin, B., Chen, T., Pu, X., Liu, W., & Peng, M. (1986). Rupture processes of strong earthquakes on Xianshuihe fault belt and seismic activity. *Acta Seismologica Sinica*, 8(1), 1–20. (in Chinese)

Lisiecki, L.E., & Raymo, M.E. (2005). A Pliocene–Pleistocene stack of 57 globally distributed benthic δ18O records. *Paleoceanography, 20*, PA1003. Doi:10.1029/2004PA001071

Liu, Z., Zhang, G., Hu, Y., & Yang, Y. (1977). Geological map of Gongga (H-47-24). Sichuan Institute of Geology, Scale 1/200,000

Lu, Y., Shi, R., Hu, Y., & Zhang, S. (1975). Geological map of Yingjing (H-48-19). Sichuan Institute of Geology, Scale 1/200,000

Meade, B. J., & Loveless, J. P. (2009). Block modeling with connected fault network geometries and a linear elastic coupling estimator in spherical coordinates. *Bulletin of the Seismological Society of America, 99 (6)*, 3124–3139. Doi:10.1785/0120090088

Nalbant, S.S., & McCloskey, J. (2011). Stress evolution before and after the 2008 Wenchuan, China earthquake. *Earth and Planetary Science Letters, 307,* 222–232. Doi:10.1016/j.epsl.2011.04.039

Ouimet, W.B., Whipple, K.X., & Granger, D.E. (2009). Beyond threshold hillslopes: chan-nel adjustment to base-level fall in tectonically active mountain ranges. *Geology 37*, 579–582. Doi:10.1130/g30013a.1

Pan, J., Li, H., Chevalier, M.L., Bai, M., Liu, F., Liu, D., Zheng, Y., Lu, H., & Zhao, Z. (2020). A newly discovered active fault on the Selaha-Kangding segment along the SE Xianshuihe fault: the South Mugecuo fault. *Acta Geologica Sinica, 94(11)*, 3178-3188 (in Chinese). doi: 10.19762/j.cnki.dizhixuebao.2020196

Papadimitriou, E., Wen, X., Karakostas, V., & Jin, X. (2004). Earthquake Triggering along the

Xianshuihe Fault Zone of Western Sichuan, China. *Pure applied Geophysics, 161,* 1683–1707. Doi:10.1007/s00024-003-2471-4

Parsons, T., Ji, C., & Kirby, E. (2008). Stress changes from the 2008 Wenchuan earthquake and increased hazard in the Sichuan basin. *Nature, 454,* 509–510. Doi:10.1038/nature07177

Putkonen, J., & Swanson, T. (2003). Accuracy of cosmogenic ages for moraines. *Quaternary Research, 59*, 255–261. Doi:10.1016/S0033-5894(03)00006-1.

Qiao, X., & Zhou, Y. (2021). Geodetic imaging of shallow creep along the Xianshuihe fault and its frictional properties. *Earth and Planetary Science Letters, 567,* 117001. Doi:10.1016/j.epsl.2021.117001

Roger, F., Calassou, S., Lancelot, J., Malavieille, J., Mattauer, M., Xu, Z., Hao. Z., & Hou, L. (1995). Miocene emplacement and deformation of the Konga Shan granite (Xianshui He fault zone, west Sichuan, China): Geodynamic implications. *Earth and Planetary Science Letters, 130,* 201–216. Doi:10.1016/0012-821X(94)00252-T

Searle, M.P., Roberts, N.M.W., Chung, S.-L., Lee, Y., Cook, K.L., Elliott, J.R., Weller, O.M., St-Onge, M.R., Xu, X.-W., Tan, X.-B., & Li, K. (2016). Age and anatomy of the Gongga Shan batholith, eastern Tibetan Plateau, and its relationship to the active Xianshuihe fault. *Geosphere, 12 (3)*, 948–970. Doi:10.1130/ges01244.1

Segall, P., & Pollard, D. (1980). Mechanics of Discontinuous Faults. *Journal of Geophysical Research, 85(B8),* 4337-4350

Shao, Z., Xu, J., Ma, H., & Zhang, L. (2016). Coulomb stress evolution over the past 200 years and seismic hazard along the Xianshuihe fault zone of Sichuan, China. *Tectonophysics, 670,* 48-65. Doi:10.1016/j.tecto.2015.12.018

Shan, B., Xiong, X., Zheng, Y., & Diao, F. (2009). Stress changes on major faults caused by Mw7.9

887 Wenchuan earthquake May 12, 2008. *Science in China*, 52, 593–601

888 Shan, B., Xiong, X., Zheng, Y., Jin, B., Liu, C., Xie, Z., & Hsu, H. (2013). Stress changes on major
889 faults caused by 2013 Lushan earthquake and its relationship with 2008 Wenchuan earthquake.
890 *Science in China - Earth Science, 56,* 1169-1176. Doi:10.1007/s11430-013-4642-1

891 Shen, Z., Lu, J., Wang, M., & Bürgmann, R. (2005). Contemporary crustal deformation around the
892 southeast borderland of the Tibetan Plateau. *Journal of Geophysical Research, 110,* B11409.
893 Doi:10.1029/2004JB003421

894 Stone, J. O. (2000). Air pressure and cosmogenic isotope production. *Journal of Geophysical*
895 *Research, 105(B10)*, 23,753–23,759. Doi:10.1029/2000JB900181

896 Tapponnier, P., & Molnar, P. (1977). Active faulting and Cenozoic tectonics of China. *Journal of*
897 *Geophysical Research, 82,* 2905-2930. Doi:10.1029/JB082i020p02905

898 Toda, S., Lin, J., Meghraoui, M., & Stein, R.S. (2008). 12 May 2008 M = 7.9 Wenchuan, China,
899 earthquake calculated to increase failure stress and seismicity rate on three major fault systems.
900 *Geophysical Research Letters*, 35, L17305. Doi:10.1029/2008GL034903

901 Wallis, S., Tsujimori, T., Aoya, M., Kawakami, T., Terada, K., Suzuki, K., & Hyodo, H. (2003).
902 Cenozoic and Mesozoic metamorphism in the Longmenshan orogen: implications for
903 geodynamic models of eastern Tibet. *Geology, 31,* 745–748. Doi:10.1130/g19562.1

904 Wang, E., Burchfiel, B. C., Royden, L. H. Chen, L., Chen, J., Li, W., & Chen, Z. (1998). The
905 Cenozoic Xianshuihe– Xiaojiang, Red River, and Dali fault systems of southwestern Sichuan
906 and central Yunnan, China. *Geological Society of America Special Paper, 327,* 108p.
907 Doi:10.1130/SPE327

908 Wang, E., & Burchfiel, B.C. (2000). Late Cenozoic to Holocene deformation in southwestern
909 Sichuan and adjacent Yunnan, China, and its role in formation of the southeastern part of the

910 Tibetan Plateau. *Geological Society of America Bulletin, 112*, 413–423. Doi:10.1130/0016-
911 7606(2000)112<413:LCTHDI>2.0.CO;2

912 Wang, H., Wright, T.J., & Biggs, J. (2009). Interseismic slip rate of the northwestern Xianshuihe
913 fault from InSAR data. *Geophysical Research Letters, 36,* L03302.
914 Doi:10.1029/2008GL036560

915 Wang, S., Jiang, G., Xu, T., Tian, Y., Zheng, D., & Fang, X. (2012). The Jinhe–Qinghe fault—
916 Aninactive branch of the Xianshuihe–Xiaojiang fault zone, Eastern Tibet. *Tectonophysics, 544-*
917 *545,* 93-102. Doi:10.1016/j.tecto.2012.04.004

918 Wang, W., Qiao, X., Yang, S., & Wang, D. (2017). Present-day velocity field and block kinematics
919 of Tibetan Plateau from GPS measurements. *Geophysical Journal International, 208*, 1088-
920 1102. Doi:10.1093/gji/ggw445

921 Wang, Y., Wang, M., & Shen, Z. (2017). Block-like versus distributed crustal deformation around
922 the northeastern Tibetan plateau. *Journal of Asian Earth Sciences, 140*, 31-47.
923 Doi:10.1016/j.jseaes.2017.02.040

924 Wang, W., Qiao, X., & Ding, K. (2020). Present-day kinematics in southeastern Tibet inferred from
925 GPS measurements. *Journal of Geophysical Research,* e2020JB021305.
926 Doi:10.1029/2020JB021305

927 Wang, M., & Shen, Z. (2020). Present-day crustal deformation of continental China derived from
928 GPS and its tectonic implications. *Journal of Geophysical Research, 125,* e2019JB018774.
929 Doi:10.1029/2019JB018774

930 Wells, D.L., & Coppersmith, K.J. (1994). New empirical relationships among magnitude, rupture
931 length, rupture width, rupture area, and surface displacement. *Bulletin of the Seismological*
932 *Society of America, 84*, 974–1002

933 Wen, X. (2000). Character of rupture segment of Xianshuihe- Zemuhe–Anninghe fault zone,
934 western Sichuan. *Seismology and Geology, 22*, 239–249

935 Wen, X., Ma, S., Xu, X., & He, Y. (2008). Historical pattern and behavior of earthquake ruptures
936 along the eastern boundary of the Sichuan–Yunnan faulted-block, southwestern China. *Physics*
937 *of the Earth and Planetary Interiors, 168 (1–2)*, 16–36. Doi:10.1016/j.pepi.2008.04.013

938 Wilson, C.J.L., & Fowler, A.P. (2011). Denudational response to surface uplift in east Tibet:
939 evidence from apatite fission-track thermochronology. *Geological Society of America Bulletin,*
940 *123*, 1966–1987. Doi:10.1130/b30331.1

941 Xie, Z., Zheng, Y., Liu, C., Shan, B., Riaz, M. S., & Xiong, X. (2017). An integrated analysis of
942 source parameters, seismogenic structure, and seismic hazards related to the 2014 M S 6.3
943 Kangding earthquake, China. *Tectonophysics, 712,* 1-9. Doi:10.1016/j.tecto.2017.04.030

944 Xu, G., & Kamp, P.J.J. (2000). Tectonics and denudation adjacent to the Xianshuihe Fault, eastern
945 Tibetan Plateau: constraints from fission track thermochronology. *Journal of Geophysical*
946 *Research, 105,* 19231–19251.Doi:10.1029/2000jb900159

947 Xu, J., Shao, Z., Ma, H., & Zhang, L. (2013). Evolution of Coulomb stress and stress interaction
948 among strong earthquakes along the Xianshuihe fault zone. *Chinese Journal of Geophysics,*
949 *56(4)*, 1146-1158 (in Chinese). Doi:10.6O38/cjg2O13O41O

950 Xu, J., Shao, Z., Liu, J., & Ji, L. (2019). Coulomb stress evolution and future earthquake
951 probability along the eastern boundary of the Sichuan-Yunnan block. *Chinese Journal of*
952 *Geophysics*, *62(11)*, 4189-4213 (in Chinese)

953 Yan, B., & Lin, A. (2015). Systematic deflection and offset of the Yangtze River drainage system
954 along the strike-slip Ganzi-Yushu-Xianshuihe Fault Zone, Tibetan Plateau. *Journal of*
955 *Geodynamics, 87,* 13-25. Doi:10.1016/j.jog.2015.03.002

Yan, B., & Lin, A. (2017). Holocene Activity and Paleoseismicity of the Selaha Fault, Southeastern Segment of the Strike-Slip Xianshuihe Fault Zone, Tibetan Plateau. *Tectonophysics, 694(2),* 302–318. Doi:10.1016/j.tecto.2016.11.014

Yan, B., Jia, D., & Lin, A. (2018). Late Pleistocene-Holocene tectonic landforms developed along the strikeslip Xianshuihe Fault Zone, Tibetan Plateau, China. *Journal of Geodynamics, 120*, 11–22. Doi:10.1016/j.jog.2018.05.005

Yan, B., Wang, M., Jia, D., & Cui, J. (2019). Investigation and magnitude re-evaluation of the 1955 Zheduotang earthquake, eastern Tibetan Plateau, China. *Geological Journal, 2019,* 1–13. Doi:10.1002/gj.3628

Yang, W., Cheng, J., Liu, J., & Zhang, X. (2015). The Kangding earthquake swarm of November, 2014. *Earthquake Science, 28(3)*, 197-207. Doi:10.1007/s11589-015-0123-2

Zechar, J.D., & Frankel, K.L. (2009). Incorporating and reporting uncertainties in fault slip rates. *Journal of Geophysical Research, 114*, B12407. Doi:10.1029/2009JB006325

Zhang, Y., Chen, W., & Yang, N. (2004). 40Ar/39Ardating of shear deformation of the Xianshuihe fault zone in west Sichuan and its tectonic significance. *Science in China, 47*, 794–803. Doi:10.1360/03yd0509

Zhang, P.Z. (2013). A review on active tectonics and deep crustal processes of the Western Sichuan region, eastern margin of the Tibetan Plateau. *Tectonophysics, 584,* 7-22. Doi:10.1016/j.tecto.2012.02.021

Zhang, Y., Replumaz, A., Leloup, P.H., Wang, G., Bernet, M., van der Beek, P., Paquette, J.L. & Chevalier, M. L. (2017). Cooling history of the Gongga batholith: implications for the Xianshuihe Fault and Miocene kinematics of SE Tibet. *Earth and Planetary Science Letters, 465,* 1-15. Doi:10.1016/j.epsl.2017.02.025

979 Zhang, L., Cao, D., Zhang, J., & Sui, L. (2019). Interseismic Fault Movement of Xianshuihe Fault
980 Zone Based on Across-Fault Deformation Data and InSAR. *Pure and Applied Geophysics,*
981 *176*, 649–667. Doi:10.1007/s00024-018-1989-4

982 Zheng, G., Wang, H., Wright, Tim J., Lou, Y., Zhang, R., Zhang, W., Shi, C., Huang, J., & Wei, N.
983 (2017). Crustal deformation in the India-Eurasia collision Zong from 25 years of GPS
984 measurements. *Journal of Geophysical Research, 122*, 9290–9312.
985 Doi:10.1002/2017JB014465

986 Zhou, R., He, Y., Huang, Z., Li, X., & Yang, Z. (2001). The slip rate and recurrence of strong
987 earthquakes of Qianning-Kangding segment, the Xianshuihe fault zone. *Acta Seismologica*
988 *Sinica, 23(3),* 250-261 (in Chinese)

989

990 **Figure Captions for Supplementary material:**

991 **Figure S1.** Photos of boulders collected for ^{10}Be surface-exposure dating at the ZDT
992 moraine site with their approximate sizes.

993

994 **Figure S2:** Photos of boulders collected for ^{10}Be surface-exposure dating along the MX main
995 moraine with their approximate sizes.